Lung injury induces alveolar type 2 cell hypertrophy and polyploidy with implications for repair and regeneration

Anthea Weng[1], Mariana Maciel-Herrerias[1], Satoshi Watanabe[1], Lynn Welch[1], Annette S. Flozak[1], Rogan Grant[1], Raul Piseaux Aillon[1], Laura Dada[1], Seung Hye Han[1], Monique Hinchcliff[3], Alexander Misharin[1], GR Scott Budinger[1], Cara J. Gottardi[1,2]*

Northwestern University, Feinberg School of Medicine
[1]Department of Pulmonary Medicine, [2]Biochemistry and Molecular Genetics
Chicago, IL 60611, USA

[3]Department of Medicine, Division of Rheumatology, Allergy and Immunology, Yale University School of Medicine
New Haven, CT 06510 USA

Running title: Injury-induced alveolar epithelial polyploidization

Corresponding author*:
Cara J. Gottardi
303 East Superior Street
Simpson-Querrey 5-525
Chicago, IL 60611, USA
c-gottardi@northwestern.edu
312-503-4123

4636 words (Abstract, Results, Discussion, Figure legends; minus Methods or References)
7 Figures; 5 supplements (4 figures plus 1 video)

Abstract (135)

Epithelial polyploidization post-injury is a conserved phenomenon, recently shown to improve barrier restoration during wound healing. Whether lung injury can induce alveolar epithelial polyploidy is not known. We show that bleomycin injury induces AT2 cell hypertrophy and polyploidy. AT2 polyploidization is also seen in short term ex vivo cultures, where AT2-to-AT1 trans-differentiation is associated with substantial binucleation due to failed cytokinesis. Both hypertrophic and polyploid features of AT2 cells can be attenuated by inhibiting the integrated stress response (ISR) using the small molecule ISRIB. These data suggest that AT2 hypertrophic growth and polyploidization may be a feature of alveolar epithelial injury. As AT2 cells serve as facultative progenitors for the distal lung epithelium, a propensity for injury-induced binucleation has implications for AT2 self-renewal and regenerative potential upon re-injury, which may benefit from targeting the ISR.

Keywords: Alveolar epithelial cell, injury, hypertrophy, binucleation, polyploidy, cytokinesis, integrated stress response

Introduction

Genome wide association and classical genetic studies of families with pulmonary fibrosis implicate disordered epithelial repair as a driver of lung fibrosis (1-3). While this hypothesis has been confirmed in mouse models of fibrosis that localize fibrosis-promoting effects of global mutations to the lung epithelium (4-6), the sequence of cellular events that drive fibrosis persistence remains unclear. Understanding how the distal lung epithelium repairs after injury is also relevant to patients with severe lung injury induced by SARS-CoV-2 pneumonia, where some will develop persistent and progressive lung fibrosis (7-12). Thus, while it is clear surfactant producing-alveolar type 2 pneumocytes (AT2 cells) are progenitors that give rise to alveolar type 1 pneumocytes (AT1 cells)(13, 14), the variability between individuals in the AT2-to-AT1 cell trans-differentiation program to restore normal alveolar function is unexplained.

Pathologists have long recognized that a range of injurious stimuli lead to the accumulation of abnormally large AT2 cells, described as “hypertrophic or hyperplastic” AT2 cells (15-18). Morphologically similar cells are seen in autopsy specimens or lung explants from patients with lung injury secondary to SARS-CoV-2 pneumonia (7, 11, 19), but mechanisms underlying this cell state and its consequences for lung repair post-injury remain puzzling. A recent convergence of single cell transcriptomic-studies from a range of mouse injury models suggests that instead of fully progressing to an AT1 cell fate, AT2 cells become stalled at an intermediate transition-state characterized by activation of cell cycle arrest pathways (p16, p21, p53),TGFβ signaling and matrix remodeling (SERPINE1)(20-23). Serially collected single cell RNA-sequencing data over the course of bleomycin induced injury shows the formation of this intermediate transition state is preceded by increased expression of genes in the integrated stress response (ISR)(22). In tissue sections, these transitional cells are characterized by elevated levels of specific intermediate filament keratins (KRT8/18 in mice; KRT17 in humans) and other structural proteins, along with an intermediate AT2-to-AT1 morphology (22, 23). These data suggest small cuboidal AT2 cells differentiate into large and flattened AT1 cells through a morphologically stressful transition that appears prone to stalling after injury. Importantly, recent evidence suggests the AT2-to-AT1 transition state is not fixed, as therapeutic targeting of p53 or ISR signaling appears to guide AT2 cells through this vulnerable trans-differentiation step (23, 24). However, the cellular processes most vulnerable to this morphogenetic transition, which drive persistence of the AT2-to-AT1 transition state in injured lungs and can be reversed by these therapies are unknown.

82 Epithelial polyploidization and consequent hypertrophy post-injury is a conserved phenomenon
83 observed from flies to vertebrates (25). It is a process by which cells increase their DNA content
84 and bypass mitosis. Polyploid cells are larger than their diploid counterparts because cell size
85 scales with DNA content (26). Cell hypertrophy is advantageous during epithelial repair, as
86 larger cells manifest less junctional surface area per unit of epithelium, leading to decreased
87 permeability in an otherwise leaky-barrier environment (27, 28). Increased DNA copies can also
88 favor adaptation to cell and environmental stress, in ways that are context and injury dependent
89 (29-31). However, these benefits of polyploidization come at a cost, as polyploid cells will less
90 faithfully segregate DNA during mitosis (32-34). Thus, polyploidization of differentiated cell
91 types—particularly those that serve also as progenitors (e.g., AT2 cells)—is likely to adversely
92 impact future regenerative potential of the tissue. Whether AT2 polyploidy underlies injury-
93 induced AT2 hypertrophy, or is a consequence of hypertrophic growth, and drives persistence of
94 the AT2-to-AT1 cell stalled state is unknown.
95
96 In this study, we show that lung injury leads to AT2 hypertrophy and polyploidization—notably
97 binucleated AT2s—during the acute injury response. *Ex vivo* analysis suggests the route to
98 polyploidy is via failed cytokinesis during the AT2-to-AT1 flattening process. A small molecule
99 inhibitor of the integrated stress response, ISRIB, which we have previously shown ameliorates
100 fibrosis development in murine models (24), inhibits the abundance of hypertrophic and
101 polyploid AT2 cells. These data suggest that modulating stress signals during the
102 morphogenetically challenging AT2-to-AT1 transition may improve key steps through which
103 injured AT2 cells divide and differentiate to restore the alveolar epithelium. Implications of failing
104 to remove and replace polyploid AT2 cells after lung injury are discussed.

Results

Lung injury induces AT2 hypertrophy

To understand how lung injury alters the morphogenetic sequence by which AT2 cells grow, divide and differentiate to an AT1 fate, we used a genetic lineage tracing system to permanently label AT2 cells in *Sftpc*$^{Cre\text{-}ER}$; $^{Lox\text{-}Stop\text{-}Lox}$zsGreen mice subjected to the bleomycin model of injury and fibrogenic repair (24) (Fig.1A). As with previous studies (15-18), we confirm that bleomycin injury leads to zsGreen+ cells that are larger than AT2 lineage-labeled mice exposed to saline (Fig. 1B and C, quantification from 2 mice, 5 fields of view; Frozen section image analysis pipeline in Fig. S1A). Cell size difference may be more readily apparent in 14μm thick frozen sections than thinner 4μm paraffin sections, likely because the former method favors cell visualization along a greater portion of the curved alveolus (Fig. S1B). The injury-induced size increase is not an aberrant feature of cells expressing the fluorescence lineage-label, as AT2 cells lacking zsGreen but expressing surfactant protein C (SpC) also increase in size (Fig. S1C). Since standard sectioning (i.e., planimetry) is known to underestimate AT2 cell expansion post-injury (35, 36), we also confirmed AT2 hypertrophic growth using cleared, thick-section (200μm) confocal imaging with 3-dimensional reconstruction (Fig. 1D, quantification from 3 mice; Video 1). Lastly, we can detect this size increase by flow cytometric analysis of AT2 cells (Fig. S2A-C; Median Forward Scatter Area quantification from 3 mice/condition), demonstrating the injury-induced phenotype is not likely an artefact of lung fixation or processing.

Lung injury promotes AT2 cell polyploidization

As cell size can scale with DNA context (26), we sought to examine nuclear features of hypertrophic AT2 cells. Interestingly, we found a number of lineage-labeled AT2 cells with two nuclei (Fig. 2A), often observing 1-2 binucleated zsGreen+ cells per field of view, estimating a rate of ~8% (Fig. 2B; see also Fig.1B inset box). To validate AT2 polyploidy via an independent method, we sought to quantify and characterize these cells by flow cytometry paired with DNA content analysis (Fig. S2A-E). Although we readily detected AT2 cells with 2N or 4N DNA content, too few 4N cells survived the cytospin procedure to reliably quantify binucleation rate differences between saline and bleomycin-treated mice (Fig. S2E). Methodological improvements will be required to reliably isolate and quantify this apparently fragile cell state, particularly given that flow cytometry is known to underestimate expansion of AT2 numbers post-injury (35).

137 Of interest, AT2 binucleation appears compatible with expression of the AT2 marker, surfactant
138 protein C (SpC) (Fig. S2F), as well as the AT1 marker, podoplanin (Fig. 6D; *ex vivo* AT2 cell
139 cultures). Together with recent evidence that genetically-induced AT2 binucleation is compatible
140 with Hopx expression (37), these data suggest alveolar epithelial polyploidy may be compatible
141 with either AT2 or AT1 cell state. To address whether AT2 polyploidy is a typical feature of the
142 recently described AT2-to-AT1 cell transition state (21, 22), we interrogated Krt8 expression in
143 our lung sections. While we can find large binucleated cells that highly express Krt8 protein,
144 AT2 binucleation does not exclusively correlate with a Krt8-high state (Fig. 3). Remarkably,
145 binucleation is a common feature of primary AT2 cultures grown on glass or filters (Fig. 4). We
146 are confident these *ex vivo* polyploid cells derive from *bona fide* AT2 cells, as they are uniformly
147 Krt8-positive (Fig. 4A) and can be lineage-labeled using the *Sftpc*-$^{\text{CreER; Lox-stop-Lox eYFP}}$ system
148 (Fig. S4A,B). Even AT2-derived organoids, which can show AT2-to-AT1 cell transition state
149 features seen in injured lungs (23), exhibit a binucleation rate similar to *in vivo* estimates (Fig.
150 4B-D vs Fig. 2B). Mechanistically, live-imaging reveals binucleated cells can be generated via
151 failed cytokinesis, further suggesting that how AT2 polyploidy is generated and maintained can
152 be interrogated in *ex vivo* cultures (Fig. 5).

153 Given limitations of assessing polyploidy from frozen or thick sectioning (Fig. S1B), together
154 with evidence that mononuclear polyploidy also exists (38), we sought an independent method
155 to assess the polyploidy rate in injured AT2 cells. A recent study showed that the stochastic,
156 multi-color Confetti reporter system can be used to assess mononuclear polyploidy in mouse
157 tissues, notably liver (39). While the Confetti reporter mouse is better known for tracing clonal
158 cell relationships in development and injury (14, 40), this tool can also validate polyploid cells in
159 tissues with single cells expressing two or more fluorescent proteins (Fig. S3A). In contrast to
160 cell clone tracing, the lineage label must be activated by tamoxifen *after genome duplication* to
161 detect single cell polyploidy. By subjecting *Sftpc*$^{\text{Cre-ER}}$ x *Rosa*^{Confetti} mice to the bleomycin model
162 of injury, we could identify large, partially flattened cells that express both green fluorescent
163 protein (GFP) and red fluorescent protein (RFP) lineage labels surrounding what appears as a
164 single nucleus of lineage-label exclusion (Fig. S3B,C). We also identified small round,
165 GFP/RFP-dual-positive cells that likely reflect lineage-labeled AT2 cells which have doubled
166 their DNA content and arrested at the G2-phase of the cell cycle (Fig. S3D). As these dual-
167 positive cells appear more rare than the AT2 binucleation rate estimated in Figure 1 (e.g., < 2%
168 lineage-labelled AT2 cells), we may be missing polyploidization events during the AT2-to-AT1
169 transition, when *Sftpc*^{Cre}-expression is likely waning. Crossing the *Rosa*^{Confetti}-reporter strain to a
170 Cre-driver whose expression increases during the AT2-to-AT1 transition may be required to

171 assess the full extent of alveolar epithelial polyploidization during the lung injury-repair
172 sequence. Nonetheless, these data show that lung injury can generate binucleated polyploid
173 AT2 cells (Fig. 1), and possibly polyploid mononuclear AT2 cells (Fig. S3C), where
174 polyploidization likely occurs during the post-injury, reparative phase of the bleomycin model.
175

176 **Inhibiting the Integrated Stress Response attenuates AT2 hypertrophy**

177 To determine whether injury-induced AT2 hypertrophy and polyploidy can be inhibited or
178 reversed, we considered small molecule approaches known to target stress-activated pathways,
179 recently suggested to guide injured AT2 cells through their vulnerable transition towards an AT1
180 fate (23, 24). The integrated stress response (ISR) is a highly conserved signaling network that
181 helps cells adapt to a range of environmental stresses, through activating kinases that inhibit
182 bulk protein translation in favor of the translation of select mRNAs encoding transcription factors
183 such as ATF4 that promote the transcription of molecular chaperones and other stress adaptive
184 genes (41). A central integrator of these diverse stress-responsive kinases is the eIF2
185 complex, where phosphorylation of eIF2α at a single serine residue limits translation (42). In this
186 way, eIF2α phosphorylation and its diverse downstream consequences comprise the ISR (43,
187 44). A small molecule integrated stress response inhibitor, ISRIB, was found to render cells
188 insensitive to eIF2α phosphorylation, thereby restoring translation capacity to normalize cell
189 function (45-47) and limit a range of tissue pathologies in murine disease models (48-51). Our
190 team recently discovered that ISRIB reduces fibrosis in mouse models (24). Since ISRIB
191 therapy limited abundance of lineage-labelled AT2 cells co-expressing KRT8, yet increased
192 abundance of lineage-labeled cells expressing podoplanin, we reason that ISRIB may attenuate
193 fibrosis by limiting abundance of AT2 cells stalled at the AT2-to-AT1 transition state, favoring
194 their full transition to an AT1 fate (24). Indeed, evidence that bleomycin-injured AT2 cells show
195 activation of ISR-associated genes during this transdifferentiation step (24), further suggests
196 that persistent activation of the ISR in AT2 cells can thwart alveolar epithelial repair. However,
197 the particular morphogenetic features of the AT2-to-AT1 transition that drive persistence of this
198 stress state remain unclear. We find that bleomycin-injured *Sftpc*$^{\text{Cre-ER; Lox-Stop-Lox}}$zsGreen mice
199 treated with ISRIB show complete inhibition of AT2 hypertrophy and no evidence of binucleation
200 (Fig. 6A,B). Although ISRIB did not prevent AT2 cell binucleation in *ex vivo* cell cultures, ISRIB
201 treatment did limit the rate of binucleation, as well as formation of the largest cells, inferred from
202 nuclear size within these cells (Fig. 6C-G). These data suggest that injury-induced AT2
203 hypertrophy and polyploidy are sensitive to inhibition of the ISR. Evidence for modest cell size

204 attenuation in *ex vivo* AT2 cultures suggests that ISRIB may limit hypertrophic growth through
205 an AT2 cell-autonomous mechanism.
206
207

Discussion

For decades, clinical pathologists have described the development of “hypertrophic” AT2 cells after injury, but mechanisms that drive this state and degree to which it benefits and/or constrains the lung injury-repair cycle is not known. We show that some of this hypertrophic growth is associated with AT2 polyploidy, most notably binucleated AT2 cells. *Ex vivo* analysis suggests the route to polyploidy is via failed cytokinesis during the AT2-to-AT1 flattening process. Remarkably, attenuating the ISR with ISRIB limits the abundance of hypertrophic, polyploid AT2 cells after bleomycin injury and *ex vivo* culture, suggesting the effects of ISRIB may be AT2 cell-autonomous. Given recent high resolution time-series sampling of the injured lung and analysis by single cell RNA-sequencing revealing that the AT2-to-AT1 transition state expresses genes associated with the ISR (22), we suggest that lung injury persistently activates the ISR in AT2 cells as they divide, enlarge and flatten to repair the alveolar epithelium, increasing their susceptibility to cytokinesis failure into polyploid AT2 cells. A key consequence of AT2 polyploidization will be loss of the AT2 stem cell daughter, which may compromise future regenerative potential of alveoli served by that AT2 progenitor. We propose that attenuating the ISR helps guide AT2 cells through this vulnerable morphogenetic sequence of cell-growth, division and trans-differentiation without polyploidy (Fig. 7, Model).

Evidence that AT2 binucleation does not exclusively correlate with cells expressing the highest levels of KRT8 protein is noteworthy. While elevated *Krt8* expression is associated with an aberrant AT2-to-AT1 transition state (21, 22), perhaps this transition is only one of a number of transcriptionally distinct routes cells take as they repair the injured alveolar epithelium. Alternatively, the Krt8-high/*Sftpc*$^{CreER;\ zsGreen}$ -negative binucleated cells detected in Figure 3B suggests alveolar epithelial polyploidization may also occur via *Sftpc*-lineage negative progenitors (52). Given the increased size and presumed fragility of polyploid alveolar cells, we suspect they are inadequately represented in current lung single cell RNA-sequencing pipelines. To understand how these cells specifically contribute to alveolar repair, it will be necessary to revise existing cell sorting pipelines to quantify the abundance and degree of alveolar epithelial polyploidy, as well as isolate these cells for downstream transcriptomic analyses to establish the distinct features of the polyploid cell state (33).

Recent injury-repair studies using live-imaging of zebrafish epicardium as a simple epithelial model system reveal that cells along a closing wound-front manifest higher tension and rates of

242 binucleation due to failed cytokinesis (28). While one study suggests this may be due to
243 excessive integrin-based extracellular matrix adhesive tension that ultimately interferes with
244 contractility of the actin-myosin cytokinetic ring (53), there are many routes to cytokinesis failure
245 caused by reduced or elevated Rho-signaling (54). Endoplasmic reticulum (ER)-stress itself
246 can lead to cytokinesis failure (55, 56). Moreover, PKR, a dsRNA-dependent Protein Kinase and
247 upstream activator of the ISR, can be activated by mitosis onset, where nuclear membrane
248 breakdown releases endogenous dsRNAs that bind and activate PKR (57). This activation is
249 required for cytokinetic fidelity, underscoring the relationship between ISR signaling and cell
250 division. Future work will be required to determine whether cytokinesis is more vulnerable to
251 ATF4-dependent versus independent arms of the ISR.
252
253 Although bleomycin-injury leads to binucleation in only ~5% of lineage-labeled AT2 cells, total
254 alveolar epithelial cell polyploidy may be much greater, particularly given evidence for
255 mononuclear polyploidy across tissues (38). Newer imaging methods that allow simultaneous
256 assessment of DNA content and cell cycle phase will be required to distinguish true
257 mononuclear polyploidy (i.e., $\geq$4N DNA content in a G_1-phase cell) from AT2 cells arrested post-
258 genome doubling at the G_2-phase (i.e., also 4N DNA content) (58). Another limitation of this
259 study is our reliance on the DNA-damaging agent bleomycin as an injury model, which could
260 bias the alveolar repair response towards AT2 polyploidy. Future work will be required to
261 determine the generality of this paradigm, and whether AT2 polyploidy can be induced by other
262 forms of injury (e.g., viral or pneumonectomy model of alveologenesis).
263
264 Conceptually, it will be important address whether AT2 polyploidization is restricted to the
265 transdifferentiating daughter, sparing normal ploidy of the renewed AT2 or if lung injury
266 promotes AT2 endocycling/endomitosis, resulting in a polyploid facultative progenitor. The
267 former would generate polyploid AT1 cells, which might allow AT1 cells to become larger with
268 excess DNA copies for environmental adaptation (25). Indeed, a recent proof-of-concept study,
269 which genetically induced cytokinesis failure in AT2 cells, found that binucleation does not
270 obviously prevent trans-differentiation towards at AT1 fate (37). These data are consistent with
271 our own evidence that binucleation is compatible with expression of the AT1-marker, podoplanin
272 (Fig. 6D). Polyploidization of AT2 cells could provide extra DNA copies for surfactant
273 biosynthesis, similar to how mammary epithelial cells become polyploid during lactation to
274 maximize milk production (30). However, the induction of AT2 polyploidy would likely
275 compromise its progenitor function, which requires faithful segregation of additional

276 chromosomes during mitosis for stem cell renewal (38). Even heart tissue, which comprises
277 large binucleated cardiomyocytes suited to contractility, relies on a low percentage of
278 mononuclear diploid progenitor cells (2-14%) to drive regeneration post-injury. Mouse strains
279 with a greater percentage of these mononuclear diploid cells (14%) recover from injury faster
280 than strains with a lower percentage (2%) (59). Given this precedence, we reason that even a
281 small percentage of AT2 cells becoming polyploid during an injury event (~5% per injury) could
282 ultimately contribute to substantial loss of AT2 progenitor renewal over a lifetime, absent
283 alternate mechanisms for AT2 progenitor replacement, such as via *Sftpc*-negative progenitors
284 (60).
285
286 It will be important to understand how alveolar epithelial cells sustain the polyploid state.
287 Forced-induction of polyploidy in retinal pigmented epithelial cells requires activation of p53
288 signaling (61). Given recent evidence that forced-activation of p53 may facilitate the AT2-to-
289 AT1 transition during lung injury (23), it is possible that induced polyploidy plays a beneficial role
290 in the earliest stages of alveolar epithelial repair. However, evidence that the integrated stress
291 response inhibitor, ISRIB, attenuates formation or duration of hypertrophic alveolar epithelial
292 cells (this study) and promotes lung repair in the bleomycin model (24), raises the possibility
293 that maintaining polyploid cells for too long may be detrimental.
294
295 AT2 hypertrophic growth not associated with polyploidy may also be problematic for the injury-
296 repair sequence. Young cells manipulated to grow to a large size, even without a corresponding
297 increase in DNA content (i.e., polyploidy), can manifest phenotypes observed in senescent cells
298 (62, 63). Conversely, older cells are associated with volume increase, raising the possibility that
299 cytoplasmic dilution of key factors may contribute to senescence-associated phenotypes (62).
300 Indeed, this same research team found that cell size is a determinant of stem cell
301 (hematopoietic) potential during aging, where cell enlargement contributes to functional decline
302 (64). Thus, hypertrophic growth independent of polyploidy can be maladaptive. Since most of
303 our lineage labeled AT2 cells show size increase post-injury, whereas the binucleation rate is
304 only ~5%, absent substantially higher levels of mononuclear polyploidy, it is likely that AT2
305 hypertrophy and ISR activation are upstream of and causal to the polyploidization step (Fig. 7).
306 We speculate, therefore, that an inappropriately timed hypertrophic growth spurt may interfere
307 with successful completion of mitosis. We hypothesize that ISRIB limits hypertrophic growth
308 (and polyploidy) through an ATF4-dependent or independent (i.e., bulk-translation) mechanism,
309 which can be addressed using existing ATF4 gain- and loss-of-function mice. Ultimately,

310 adaptive or maladaptive functions of hypertrophic normal (2N) versus polyploid (≥4N) AT2 cells
311 will be informed by transcriptomic studies that consider DNA content as a variable.
312 The lung needs to repair in a manner that does not massively increase cell numbers (65).
313 Epithelial polyploidization post-injury may be a way to repair such tissues where excessive
314 cellularity may be problematic. Epithelial polyploidization consequent to injury is a process with
315 short-term benefits (e.g., larger cells with enhanced barrier function/reduced leak, increased
316 DNA copies for adaptation to stressful environments), but long-term consequences (e.g.,
317 reduced stem cell maintenance due to loss of self-renewed mononuclear AT2). Our data raise
318 the possibility that modulators of the ISR may be leveraged to maintain AT2 progenitor function
319 during injury. Future work will be required to understand the means by which ISRIB limits
320 formation of or guides the transition of hypertrophic, polyploid AT2 cells towards an AT1
321 phenotype, and degree to which induced polyploidy contributes to alveolar epithelial cell
322 heterogeneity or adaptation in lung disease.
323
324
325
326
327
328
329
330
331
332
333
334

335 **Materials and Methods**

336

337 **Key resources Table**

REAGENT or RESOURCE	SOURCE	IDENTIFIER
Antibodies		
Rat anti-mouse I-A/I-E (MHC II), BUV395	BD Biosciences	Cat#743876, RRID:AB_2741827
Rat anti-mouse CD45, APC	BioLegend	Cat#102410
Rat anti-mouse CD31, APC	BioLegend	Cat#103112
Rat anti-mouse CD326 (Ep-CAM), PE/Cy7	BioLegend	Cat#118216
Rat anti-mouse CD11c, PE/Cy7	BioLegend	Cat#117318
Propidium Iodide	ThermoFisher Scientific	Cat#P1304MP
Biotin Rat Anti-mouse CD16/32	BD Biosciences	Cat#553143
Biotin Rat Anti-mouse TER119/Erythroid Cells	BD Biosciences	Cat#553672
Biotin Rat Anti-mouse CD45	BD Biosciences	Cat#553078
Biotin Rat Anti-mouse CD90	BD Biosciences	Cat#554896
Anti-Prosurfactant Protein C (proSP-C)	Millipore Sigma	Cat#AB3786
Anti-β-catenin	Millipore Sigma	Cat#06-734
Anti-β-catenin	BD Biosciences	Cat#610153
Podoplanin	DSHB (University of Iowa)	Cat#8.1.1, RRID:AB_531893
Krt8	DSHB (University of Iowa)	Cat#TROMA-I, RRID:AB_531826
Alexa Fluro 680 Phalloidin	Invitrogen	Cat#A22286
Goat anti-rabbit Alexa Fluor 488	Invitrogen	Cat#A11008
Goat anti-mouse Alexa Fluor 568	Invitrogen	Cat#A11004
Goat anti-hamster Alexa Fluor 594	Invitrogen	Cat#A21113
Goat anti-rat Alexa Fluor 546	Invitrogen	Cat#A11081
Chemicals, Peptides, and Recombinant Proteins		
Bleomycin	Fresenius Kabi	Cat#0703-3154-01
0.9% saline chloride	BBraun	Cat#R5201-01
ISRIB	AdooQ BioScience	Cat#A14302
Tamoxifen	Sigma	Cat#T5648
Corn oil	Sigma	Cat#C8267
Vybrant DyeCycle Violet Stain	Invitrogen	Cat#V35003
Hoechst 33342	ThermoFisher Scientific	Cat#62249
Draq5	ThermoFisher Scientific	Cat#62251
ROCK1 inhibitor Y-27632	Selleckhem	S1049
ProLong Gold Antifade Mountant	ThermoFisher Scientific	Cat#P36934
Eriochrome black	Sigma	Cat#E2377
CD326 (EpCAM) Microbeads, mouse	Miltenyi Biotec	Cat#130-105-958
Matrigel	Corning	Cat#356231
Collagenase	Millipore Sigma	Cat#C0130
Elastase	Worthington	Cat#LS002292

Deoxyribonuclease (DNase) I	Sigma	Cat#D4513
Dispase	Corning	Cat#47743-724
PharmLyse (Red Blood Cell Lysis)	BD Biosciences	Cat#555899
Purified Rat Anti-mouse CD16/CD32 (Mouse FcBlock)	BD Biosciences	Cat#553142
Streptavidin MagneSphere Paramagnetic Particles	Promega	Cat#Z548C
Mouse CD45 MicroBeads	Miltenyi Biotec	Cat#130-052-301
autoMACS Running Buffer – MACS Separation	Miltenyi Biotec	Cat#130-091-221
Critical Commercial Assays		
SHIELD	LifeCanvas Technologies	Cat#EI-Z1001,#SH-BS,#SH-ES,#SH-ON
MultiMACS Cell24 Separator	Miltenyi Biotec	
Experimental Models: Organisms/Strains		
Mouse: C57BL/6J (8-12 weeks old)	The Jackson Laboratory	JAX: 000664
Mouse: *Sftpc*^{CreER}	The Jackson Laboratory	JAX: 020940
Mouse: R26R^{ZsGreen}	The Jackson Laboratory	JAX: 007906
Mouse: *Sftpc*^{CreER}	International Mouse Strain Resource	MGI: 5444645
Mouse: R26R^{eYFP}	The Jackson Laboratory	JAX: 006148
Mouse: R26R^{Confetti}	The Jackson Laboratory	JAX: 013731
Software and Algorithms		
FIJI/ImageJ (version: 2.1.0/1.53c)	Schneider, CA et al., 2012	https://imagej.nih.gov/ij/
Stardist plugin	Schmit, U et al., 2018	Cell/nuclear size quantification https://arxiv.org/abs/1806.03535
Imaris		https://imaris.oxinst.com/
Other		
Vibratome	Leica Microsystems	VT1200s
Cryostat	Reichert-Jung	Cryocut 1800
W1 Spinning Disk Confocal	Nikon Instruments	
BioStation CT or other	Nikon Instruments	
Axioplan2 epifluorescence microscope	Zeiss; 20x objective (Air)	AxioCAM HR Camera with AxioVision 4.8 software
A1R Confocal	Nikon Instruments	

338

339

340 **Methods Details**

341 **Mice:** C57BL/6 mice were obtained from Jackson laboratories (Jax stock 000664). *Sftpc*^{CreER}
342 (52), Ai6-R26^{zsGreen}, *Sftpc*$^{CreERT2;R26ReYFP}$ (kindly provided by Ed Morrisey, University of
343 Pennsylvania)(66, 67) and *Sftpc*$^{CreER;R26R\text{-}Confetti}$ (14) (Jax stocks 028054, 007906, 006148,
344 013731). Only male mice were used in bleomycin-injury experiments based on established
345 injury severity in males relative to females, which improves dynamic range of assays for
346 comparisons (68). Eight to twelve week old mice were used as young adult mice. All
347 experimental protocols were approved by the Institutional Animal Care and Use Committee at
348 Northwestern University (Chicago, IL, USA). All strains including wildtype mice are bred and
349 housed at a barrier- and pathogen-free facility at the Center for Comparative Medicine at
350 Northwestern University.
351

352 **Cre recombination, bleomycin administration, ISRIB administration**

353 For nuclear activation of Cre-ER, tamoxifen was dissolved in sterile corn oil at 10 mg/100μL and
354 administered via oral gavage once a day for two days to induce Cre-recombination of floxed
355 alleles for lineage-tracing. For bleomycin injury, mice were anesthetized and intubated prior to
356 the intratracheal administration of bleomycin (0.025 units in 50μL 0.9% saline). Lungs were
357 harvested at indicated time points for downstream analyses (e.g., fixation and frozen sectioning
358 for immunofluorescence analysis, AT2 cell isolation by negative selection (69) or EpCam+
359 selection (70) and flow cytometry methods (24, 71) with modifications (below). ISRIB (AdooQ
360 BioScience, A14302) was first reconstituted in DMSO to the concentration 4mg/mL and then
361 further diluted using PBS to a final concentration of 0.3125 mg/mL (72). ISRIB was prepared at
362 2.5 mg/kg and administered daily through intraperitoneal injection in a volume of 200μL. Control
363 animals were treated with vehicle (DMSO/PBS) alone.
364

365 **Tissue preparation, AT2 isolation, flow cytometry and sorting:** Tissue preparation for AT2
366 isolation and analyses was performed as described (24, 71), with modifications. Briefly, mice
367 were euthanized and lungs were perfused through the right ventricle with 10ml of HBSS. Lungs
368 were removed and infiltrated with dispase and 0.2 mg/ml DNase I dissolved in HBSS with Ca^{2+}
369 and Mg^{2+}, using syringe with 30G needle. Lungs were chopped with scissors and incubated in
370 DMEM containing 5% FBS for 45 minutes with agitation. The tissue suspension was filtered
371 through a 70 μM strainer and washed in 10 mL media (DMEM; 5% FBS). The pellet was then
372 suspended in red blood cell (RBC) lysis buffer for 1 minute, washed with media, and filtered
373 through 40 μM strainer. The cells were incubated with EpCAM magnetic beads and AT2 were

374 collected using the MultiMACS Cell24 Separator (Miltenyi Biotec). Automated cell counting was
375 performed using Nexcelom K2 Cellometer with AO/PI reagent. Cells were incubated with
376 FcBlock (BD Biosciences, San Jose, California), and stained with a mixture of fluorochrome-
377 conjugated antibodies, as listed above. DNA content was quantified using Vybrant DyeCycle
378 Violet. Single color controls were prepared using BD CompBeads (BD Biosciences, San Jose,
379 California) and Arc beads (Invitrogen, Waltham, Massachusetts). Flow cytometry and cell
380 sorting were performed at the Northwestern University Robert H. Lurie Comprehensive Cancer
381 Center Flow Cytometry Core facility (Chicago, Illinois). Data were acquired on a custom BD
382 FACSymphony instrument using BD FACSDiva software (BD Biosciences, San Jose,
383 California). Compensation and analysis were performed using FlowJo software (TreeStar). Each
384 cell population was identified using sequential gating strategy. The percentage of cells in the
385 live/singlets gate was multiplied by the number of live cells using Cellometer K2 Image
386 cytometer to obtain cell counts. Cell sorting was performed using BD FACSAria III instrument
387 using 100μm nozzle and 40 psi pressure. *Cytospin*: Following AT2 sorting, collected cells were
388 spun at 300g for 10 minutes. Following resuspension in PBS, cells were plated onto slides.
389 Slides were spun in cytospin filters at 100g for 5 minutes followed by staining with phalloidin
390 (1:50) and Hoescht (1:10,000).
391
392 **AT2 isolation for ex vivo two-dimensional culture:** Lungs were inflated intratracheally with
393 Dispase and incubated for 45 minutes with agitation. Lungs were chopped and incubated in
394 7mL of media containing 10% FBS and DNase I (1 mg/mL) for 10 minutes. Tissue suspensions
395 were filtered through a 70μM strainer. The cell pellets were resuspended in RBC lysis buffer for
396 2 minutes. Alveolar epithelial cells were enriched through negative selection against biotinylated
397 CD16/32, CD45, CD90, and TER119 antibodies. The cell suspensions were then incubated at
398 37°C for 2 hours followed by gentle panning. Cells were counted and cultured in complete
399 media (10% FBS, 2% Penicillin and Streptomycin) onto 12mm glass coverslips. Starting 48
400 hours after isolation, cells received a daily media change either containing 0.025μM ISRIB or
401 DMSO. Cell samples were pooled from 3 mice. Rat AT2 cells were collected as previously
402 described (73). AT2 cell purity was validated by cytospin analysis (as in Fig. S2), with staining
403 for surfactant protein C, keratin 8 and vimentin; Vimentin+ cells are less than 3% and surfactant
404 protein C is expressed in ~95% of the keratin 8 population.
405
406 **AT2 organoid culture**: For organoid culture, cells were prepared as previously described (14)
407 with modifications. Mice received tamoxifen 14 days prior to isolation. AT2 isolation was

408 conducted as described above. For fibroblast isolation, lungs were inflated with 1 mL of
409 collagenase (200 U/mL), elastase (4 U/mL), and DNase solution (0.25 mg/mL). Lungs were cut
410 into pieces and incubated for 30 minutes at 37°C in digestion buffer. Lungs were processed in
411 C-tubes (Miltenyi Biotec, 130-093-237) using GentleMACS/OctoMACS dissociator (Miltenyi
412 Biotec). Suspensions were filtered through 40 μM strainer and rinsed with MACS buffer. The
413 pellet was resuspended in RBC lysis buffer, washed with MACS, and incubated with CD45
414 magnetic beads to deplete CD45+ cells. CD45- cell fraction was collected using the MultiMACS
415 Cell24 Separator (Miltenyi Biotec). Cells were sorted as described above. Following sorting,
416 $5x10^3$ zsGreen+ AT2 were mixed with $5x10^4$ fibroblasts in 50% Matrigel (Corning, 356231) and
417 50% organoid media (αMEM, penicillin/streptomycin, insulin/transferrin/selenium, FBS, heparin,
418 Amphotericin B, Rock1 inhibitor, L-glutamine) in 0.4 μM Transwell inserts. Cell/Matrigel mixtures
419 were solidified at 37°C for 5 minutes before 300μl of media was added under the Transwell. 24
420 hours after isolation, organoids received media change every other day containing either 1 μM
421 ISRIB or DMSO for 10 days.
422
423 **Tissue sectioning, immunofluorescence and image analysis:** After euthanasia and
424 perfusion, trachea was cannulated with Luer syringe stub blunt needle and mouse lungs were
425 inflated with 4% paraformaldehyde at 15 cm H_2O column pressure. Lungs were fixed in 4%
426 paraformaldehyde (PFA) overnight at 4°C followed by cryo-embedding in optimal cutting-
427 temperature compound (OCT). Sections were cut at 14μM on a cryostat. For immunostaining,
428 sections were blocked in 10% normal goat serum (NGS), 0.3%TritonX-100 in PBS for 30
429 minutes followed by an additional 1:10 anti-mouse Fab (H+L) for 2 hours. Primary antibodies
430 were prepared in 2% NGS 0.3%TritonX-100 PBS and applied to sections overnight at 4°C.
431 Sections were washed in PBS followed by secondary antibodies for 30 minutes. Lastly, sections
432 were incubated in Hoechst (1:10,000) for 5 minutes followed by a brief incubation of 0.3%
433 Eriochrome black prior to mounting. Primary antibodies were used at concentrations described
434 below. *For 2D culture*, cells were fixed 4 days after isolation in 4% PFA. For the alveolar
435 organoids, organoids were fixed 10 days after isolation. Fixed cells and organoids were
436 neutralized in 10 mM glycine followed by blocking in 10% normal goat serum (NGS) in
437 0.3%TritonX-100 PBS. Primary antibodies were prepared in 3% NGS in 0.3%TritonX-100 PBS
438 and applied for 1 hour at room temperature. Following PBS washes, fluorophore-conjugated
439 secondary antibodies were prepared at 1:300 for 30 minutes in the dark at room temperature.
440 Hoechst was diluted 1:10,000 and applied for 5 minutes at room temperature following

441 secondary antibody incubation. Coverslips and filters were mounted using ProLong Gold anti-
442 fade solution. Images were obtained using Zeiss Axioplan epifluorescence and Nikon W1
443 Spinning Disk confocal microscopes. *For nuclear area quantification*, 5 fields of view were
444 selected for each condition per biological replicate. Images were taken on a Zeiss microscope
445 and analyzed in Fiji using the Stardist plugin. Primary antibodies were as follows: SFTPC
446 (1:100); beta-catenin (1:100); Podoplanin (1:30); Krt8 (1:30), and F-actin (1:50). *For thick*
447 *section imaging with tissue clearing*, lungs were sliced in PBS using a vibratome (Leica
448 VT1200s) in 200μm thick sections. Tissue slices were cleared using the LifeCanvas
449 Technologies SHIELD method (Cambridge, MA, USA). *For 3-D volumetric analysis*, 200 μM
450 thick sections were imaged sequentially in 0.5 μM steps on a Nikon W1 Spinning Disk confocal
451 microscope. Cell volumes were measured using AT2-lineage label (YFP) via Imaris.
452
453 **Live-cell imaging:** Freshly isolated alveolar epithelial cells were plated at 500K/well in a 12 well
454 plate. 48 hours post-isolation, media was changed and adherent cells were imaged every 15-
455 minutes on a Biostation-CT system (Nikon Instruments, New York, USA) for a total of 5 hours.
456 Image sequences were analyzed in Fiji (ImageJ v: 2.1.0/1.53c).
457
458 **Statistical analysis:** Data analysis and statistical tests were performed using GraphPad Prism
459 software (v.9.2.0).
460

461 **References**

462 1. Yanagihara T, Sato S, Upagupta C, Kolb M. What have we learned from basic science
463 studies on idiopathic pulmonary fibrosis? *Eur Respir Rev* 2019; 28.
464 2. Selman M, Pardo A. The leading role of epithelial cells in the pathogenesis of idiopathic
465 pulmonary fibrosis. *Cellular signalling* 2020; 66: 109482.
466 3. Kropski JA, Blackwell TS. Progress in Understanding and Treating Idiopathic Pulmonary
467 Fibrosis. *Annu Rev Med* 2019; 70: 211-224.
468 4. Povedano JM, Martinez P, Serrano R, Tejera A, Gomez-Lopez G, Bobadilla M, Flores JM,
469 Bosch F, Blasco MA. Therapeutic effects of telomerase in mice with pulmonary fibrosis
470 induced by damage to the lungs and short telomeres. *Elife* 2018; 7.
471 5. Povedano JM, Martinez P, Flores JM, Mulero F, Blasco MA. Mice with Pulmonary Fibrosis
472 Driven by Telomere Dysfunction. *Cell Rep* 2015; 12: 286-299.
473 6. Vicary GW, Vergne Y, Santiago-Cornier A, Young LR, Roman J. Pulmonary Fibrosis in
474 Hermansky-Pudlak Syndrome. *Ann Am Thorac Soc* 2016; 13: 1839-1846.
475 7. Bharat A, Querrey M, Markov NS, Kim S, Kurihara C, Garza-Castillon R, Manerikar A,
476 Shilatifard A, Tomic R, Politanska Y, Abdala-Valencia H, Yeldandi AV, Lomasney JW,
477 Misharin AV, Budinger GRS. Lung transplantation for patients with severe COVID-19.
478 *Sci Transl Med* 2020; 12.
479 8. Bharat A, Querrey M, Markov NS, Kim S, Kurihara C, Garza-Castillon R, Manerikar A,
480 Shilatifard A, Tomic R, Politanska Y, Abdala-Valencia H, Yeldandi AV, Lomasney JW,
481 Misharin AV, Budinger GRS. Lung transplantation for pulmonary fibrosis secondary to
482 severe COVID-19. *medRxiv* 2020.
483 9. Spagnolo P, Balestro E, Aliberti S, Cocconcelli E, Biondini D, Casa GD, Sverzellati N, Maher
484 TM. Pulmonary fibrosis secondary to COVID-19: a call to arms? *Lancet Respir Med*
485 2020; 8: 750-752.
486 10. Chen J, Wu H, Yu Y, Tang N. Pulmonary alveolar regeneration in adult COVID-19 patients.
487 *Cell Res* 2020; 30: 708-710.
488 11. Delorey TM, Ziegler CGK, Heimberg G, Normand R, Yang Y, Segerstolpe A, Abbondanza
489 D, Fleming SJ, Subramanian A, Montoro DT, Jagadeesh KA, Dey KK, Sen P, Slyper M,
490 Pita-Juarez YH, Phillips D, Biermann J, Bloom-Ackermann Z, Barkas N, Ganna A,
491 Gomez J, Melms JC, Katsyv I, Normandin E, Naderi P, Popov YV, Raju SS, Niezen S,
492 Tsai LT, Siddle KJ, Sud M, Tran VM, Vellarikkal SK, Wang Y, Amir-Zilberstein L, Atri DS,
493 Beechem J, Brook OR, Chen J, Divakar P, Dorceus P, Engreitz JM, Essene A,
494 Fitzgerald DM, Fropf R, Gazal S, Gould J, Grzyb J, Harvey T, Hecht J, Hether T, Jane-
495 Valbuena J, Leney-Greene M, Ma H, McCabe C, McLoughlin DE, Miller EM, Muus C,
496 Niemi M, Padera R, Pan L, Pant D, Pe'er C, Pfiffner-Borges J, Pinto CJ, Plaisted J,
497 Reeves J, Ross M, Rudy M, Rueckert EH, Siciliano M, Sturm A, Todres E, Waghray A,
498 Warren S, Zhang S, Zollinger DR, Cosimi L, Gupta RM, Hacohen N, Hibshoosh H, Hide
499 W, Price AL, Rajagopal J, Tata PR, Riedel S, Szabo G, Tickle TL, Ellinor PT, Hung D,
500 Sabeti PC, Novak R, Rogers R, Ingber DE, Jiang ZG, Juric D, Babadi M, Farhi SL, Izar
501 B, Stone JR, Vlachos IS, Solomon IH, Ashenberg O, Porter CBM, Li B, Shalek AK,
502 Villani AC, Rozenblatt-Rosen O, Regev A. COVID-19 tissue atlases reveal SARS-CoV-2
503 pathology and cellular targets. *Nature* 2021.
504 12. McDonald LT. Healing after COVID-19: are survivors at risk for pulmonary fibrosis?
505 *American journal of physiology* 2021; 320: L257-L265.
506 13. Rock JR, Hogan BL. Epithelial progenitor cells in lung development, maintenance, repair,
507 and disease. *Annual review of cell and developmental biology* 2011; 27: 493-512.
508 14. Barkauskas CE, Cronce MJ, Rackley CR, Bowie EJ, Keene DR, Stripp BR, Randell SH,
509 Noble PW, Hogan BL. Type 2 alveolar cells are stem cells in adult lung. *The Journal of*
510 *clinical investigation* 2013; 123: 3025-3036.

15. Aso Y, Yoneda K, Kikkawa Y. Morphologic and biochemical study of pulmonary changes induced by bleomycin in mice. *Lab Invest* 1976; 35: 558-568.
16. Miller BE, Hoo KG. Regulation of phosphatidylcholine biosynthesis in activated alveolar type II cells. *American journal of respiratory cell and molecular biology* 1989; 1: 127-136.
17. Miller BE, Hook GE. Hypertrophy and hyperplasia of alveolar type II cells in response to silica and other pulmonary toxicants. *Environ Health Perspect* 1990; 85: 15-23.
18. Kasper M, Haroske G. Alterations in the alveolar epithelium after injury leading to pulmonary fibrosis. *Histol Histopathol* 1996; 11: 463-483.
19. Ting C, Aspal M, Vaishampayan N, Huang SK, Riemondy K, Wang F, Farver C, Zemans RL. Fatal COVID-19 ARDS associated with incomplete AEC1 differentiation from the transitional state without senescence or fibrosis. *bioRxiv* 2021.
20. Wu H, Yu Y, Huang H, Hu Y, Fu S, Wang Z, Shi M, Zhao X, Yuan J, Li J, Yang X, Bin E, Wei D, Zhang H, Zhang J, Yang C, Cai T, Dai H, Chen J, Tang N. Progressive Pulmonary Fibrosis Is Caused by Elevated Mechanical Tension on Alveolar Stem Cells. *Cell* 2020; 180: 107-121 e117.
21. Jiang P, Gil de Rubio R, Hrycaj SM, Gurczynski SJ, Riemondy KA, Moore BB, Omary MB, Ridge KM, Zemans RL. Ineffectual AEC2-to-AEC1 Differentiation in IPF: Persistence of KRT8(hi) Transitional State. *American journal of respiratory and critical care medicine* 2020; 201: 1443-1447.
22. Strunz M, Simon LM, Ansari M, Kathiriya JJ, Angelidis I, Mayr CH, Tsidiridis G, Lange M, Mattner LF, Yee M, Ogar P, Sengupta A, Kukhtevich I, Schneider R, Zhao Z, Voss C, Stoeger T, Neumann JHL, Hilgendorff A, Behr J, O'Reilly M, Lehmann M, Burgstaller G, Konigshoff M, Chapman HA, Theis FJ, Schiller HB. Alveolar regeneration through a Krt8+ transitional stem cell state that persists in human lung fibrosis. *Nat Commun* 2020; 11: 3559.
23. Kobayashi Y, Tata A, Konkimalla A, Katsura H, Lee RF, Ou J, Banovich NE, Kropski JA, Tata PR. Persistence of a regeneration-associated, transitional alveolar epithelial cell state in pulmonary fibrosis. *Nature cell biology* 2020; 22: 934-946.
24. Watanabe S, Markov NS, Lu Z, Piseaux Aillon R, Soberanes S, Runyan CE, Ren Z, Grant RA, Maciel M, Abdala-Valencia H, Politanska Y, Nam K, Sichizya L, Kihshen HG, Joshi N, McQuattie-Pimentel AC, Gruner KA, Jain M, Sznajder JI, Morimoto RI, Reyfman PA, Gottardi CJ, Budinger GRS, Misharin AV. Resetting proteostasis with ISRIB promotes epithelial differentiation to attenuate pulmonary fibrosis. *Proc Natl Acad Sci U S A* 2021; 118.
25. Schoenfelder KP, Fox DT. The expanding implications of polyploidy. *J Cell Biol* 2015; 209: 485-491.
26. Amodeo AA, Skotheim JM. Cell-Size Control. *Cold Spring Harb Perspect Biol* 2016; 8: a019083.
27. Cohen E, Allen SR, Sawyer JK, Fox DT. Fizzy-Related dictates A cell cycle switch during organ repair and tissue growth responses in the Drosophila hindgut. *Elife* 2018; 7.
28. Cao J, Wang J, Jackman CP, Cox AH, Trembley MA, Balowski JJ, Cox BD, De Simone A, Dickson AL, Di Talia S, Small EM, Kiehart DP, Bursac N, Poss KD. Tension Creates an Endoreplication Wavefront that Leads Regeneration of Epicardial Tissue. *Dev Cell* 2017; 42: 600-615 e604.
29. Herrtwich L, Nanda I, Evangelou K, Nikolova T, Horn V, Sagar, Erny D, Stefanowski J, Rogell L, Klein C, Gharun K, Follo M, Seidl M, Kremer B, Munke N, Senges J, Fliegauf M, Aschman T, Pfeifer D, Sarrazin S, Sieweke MH, Wagner D, Dierks C, Haaf T, Ness T, Zaiss MM, Voll RE, Deshmukh SD, Prinz M, Goldmann T, Holscher C, Hauser AE, Lopez-Contreras AJ, Grun D, Gorgoulis V, Diefenbach A, Henneke P, Triantafyllopoulou A. DNA Damage Signaling Instructs Polyploid Macrophage Fate in Granulomas. *Cell* 2016; 167: 1264-1280 e1218.

562 30. Rios AC, Fu NY, Jamieson PR, Pal B, Whitehead L, Nicholas KR, Lindeman GJ, Visvader
563 JE. Essential role for a novel population of binucleated mammary epithelial cells in
564 lactation. *Nat Commun* 2016; 7: 11400.
565 31. Wang J, Batourina E, Schneider K, Souza S, Swayne T, Liu C, George CD, Tate T, Dan H,
566 Wiessner G, Zhuravlev Y, Canman JC, Mysorekar IU, Mendelsohn CL. Polyploid
567 Superficial Cells that Maintain the Urothelial Barrier Are Produced via Incomplete
568 Cytokinesis and Endoreplication. *Cell Rep* 2018; 25: 464-477 e464.
569 32. Quinton RJ, DiDomizio A, Vittoria MA, Kotynkova K, Ticas CJ, Patel S, Koga Y,
570 Vakhshoorzadeh J, Hermance N, Kuroda TS, Parulekar N, Taylor AM, Manning AL,
571 Campbell JD, Ganem NJ. Whole-genome doubling confers unique genetic vulnerabilities
572 on tumour cells. *Nature* 2021; 590: 492-497.
573 33. Fox DT, Soltis DE, Soltis PS, Ashman TL, Van de Peer Y. Polyploidy: A Biological Force
574 From Cells to Ecosystems. *Trends Cell Biol* 2020; 30: 688-694.
575 34. Gjelsvik KJ, Besen-McNally R, Losick VP. Solving the Polyploid Mystery in Health and
576 Disease. *Trends Genet* 2019; 35: 6-14.
577 35. Jansing NL, Patel N, McClendon J, Redente EF, Henson PM, Tuder RM, Hyde DM,
578 Nyengaard JR, Zemans RL. Flow Cytometry Underestimates and Planimetry
579 Overestimates Alveolar Epithelial Type 2 Cell Expansion after Lung Injury. *American*
580 *journal of respiratory and critical care medicine* 2018; 198: 390-392.
581 36. Hsia CC, Hyde DM, Ochs M, Weibel ER, Structure AEJTFoQAoL. An official research policy
582 statement of the American Thoracic Society/European Respiratory Society: standards
583 for quantitative assessment of lung structure. *American journal of respiratory and critical*
584 *care medicine* 2010; 181: 394-418.
585 37. Liberti DC, Kremp MM, Liberti WA, 3rd, Penkala IJ, Li S, Zhou S, Morrisey EE. Alveolar
586 epithelial cell fate is maintained in a spatially restricted manner to promote lung
587 regeneration after acute injury. *Cell Rep* 2021; 35: 109092.
588 38. Ovrebo JI, Edgar BA. Polyploidy in tissue homeostasis and regeneration. *Development*
589 2018; 145.
590 39. Matsumoto T, Wakefield L, Tarlow BD, Grompe M. In Vivo Lineage Tracing of Polyploid
591 Hepatocytes Reveals Extensive Proliferation during Liver Regeneration. *Cell Stem Cell*
592 2020; 26: 34-47 e33.
593 40. Nabhan AN, Brownfield DG, Harbury PB, Krasnow MA, Desai TJ. Single-cell Wnt signaling
594 niches maintain stemness of alveolar type 2 cells. *Science* 2018; 359: 1118-1123.
595 41. Emanuelli G, Nassehzadeh-Tabriz N, Morrell NW, Marciniak SJ. The integrated stress
596 response in pulmonary disease. *Eur Respir Rev* 2020; 29.
597 42. Sudhakar A, Ramachandran A, Ghosh S, Hasnain SE, Kaufman RJ, Ramaiah KV.
598 Phosphorylation of serine 51 in initiation factor 2 alpha (eIF2 alpha) promotes complex
599 formation between eIF2 alpha(P) and eIF2B and causes inhibition in the guanine
600 nucleotide exchange activity of eIF2B. *Biochemistry* 2000; 39: 12929-12938.
601 43. Pakos-Zebrucka K, Koryga I, Mnich K, Ljujic M, Samali A, Gorman AM. The integrated
602 stress response. *EMBO Rep* 2016; 17: 1374-1395.
603 44. Costa-Mattioli M, Walter P. The integrated stress response: From mechanism to disease.
604 *Science* 2020; 368.
605 45. Sidrauski C, McGeachy AM, Ingolia NT, Walter P. The small molecule ISRIB reverses the
606 effects of eIF2alpha phosphorylation on translation and stress granule assembly. *Elife*
607 2015; 4.
608 46. Sidrauski C, Tsai JC, Kampmann M, Hearn BR, Vedantham P, Jaishankar P, Sokabe M,
609 Mendez AS, Newton BW, Tang EL, Verschueren E, Johnson JR, Krogan NJ, Fraser CS,
610 Weissman JS, Renslo AR, Walter P. Pharmacological dimerization and activation of the
611 exchange factor eIF2B antagonizes the integrated stress response. *Elife* 2015; 4:
612 e07314.

613 47. Zyryanova AF, Kashiwagi K, Rato C, Harding HP, Crespillo-Casado A, Perera LA,
614 Sakamoto A, Nishimoto M, Yonemochi M, Shirouzu M, Ito T, Ron D. ISRIB Blunts the
615 Integrated Stress Response by Allosterically Antagonising the Inhibitory Effect of
616 Phosphorylated eIF2 on eIF2B. *Mol Cell* 2021; 81: 88-103 e106.
617 48. Anand AA, Walter P. Structural insights into ISRIB, a memory-enhancing inhibitor of the
618 integrated stress response. *FEBS J* 2020; 287: 239-245.
619 49. Chou A, Krukowski K, Jopson T, Zhu PJ, Costa-Mattioli M, Walter P, Rosi S. Inhibition of the
620 integrated stress response reverses cognitive deficits after traumatic brain injury. *Proc*
621 *Natl Acad Sci U S A* 2017; 114: E6420-E6426.
622 50. Krukowski K, Nolan A, Frias ES, Boone M, Ureta G, Grue K, Paladini M-S, Elizarraras E,
623 Delgado L, Bernales S, Walter P, Rosi S. Small molecule cognitive enhancer reverses
624 age-related memory decline in mice. *bioRxiv* 2020: 2020.2004.2013.039677.
625 51. Rabouw HH, Langereis MA, Anand AA, Visser LJ, de Groot RJ, Walter P, van Kuppeveld
626 FJM. Small molecule ISRIB suppresses the integrated stress response within a defined
627 window of activation. *Proc Natl Acad Sci U S A* 2019; 116: 2097-2102.
628 52. Rock JR, Barkauskas CE, Cronce MJ, Xue Y, Harris JR, Liang J, Noble PW, Hogan BL.
629 Multiple stromal populations contribute to pulmonary fibrosis without evidence for
630 epithelial to mesenchymal transition. *Proc Natl Acad Sci U S A* 2011; 108: E1475-1483.
631 53. Uroz M, Garcia-Puig A, Tekeli I, Elosegui-Artola A, Abenza JF, Marin-Llaurado A, Pujals S,
632 Conte V, Albertazzi L, Roca-Cusachs P, Raya A, Trepat X. Traction forces at the
633 cytokinetic ring regulate cell division and polyploidy in the migrating zebrafish
634 epicardium. *Nat Mater* 2019; 18: 1015-1023.
635 54. Normand G, King RW. Understanding cytokinesis failure. *Adv Exp Med Biol* 2010; 676: 27-
636 55.
637 55. Bicknell AA, Babour A, Federovitch CM, Niwa M. A novel role in cytokinesis reveals a
638 housekeeping function for the unfolded protein response. *J Cell Biol* 2007; 177: 1017-
639 1027.
640 56. Niwa M. A cell cycle checkpoint for the endoplasmic reticulum. *Biochim Biophys Acta Mol*
641 *Cell Res* 2020; 1867: 118825.
642 57. Kim Y, Lee JH, Park JE, Cho J, Yi H, Kim VN. PKR is activated by cellular dsRNAs during
643 mitosis and acts as a mitotic regulator. *Genes Dev* 2014; 28: 1310-1322.
644 58. Zielke N, Edgar BA. FUCCI sensors: powerful new tools for analysis of cell proliferation.
645 *Wiley Interdiscip Rev Dev Biol* 2015; 4: 469-487.
646 59. Patterson M, Barske L, Van Handel B, Rau CD, Gan P, Sharma A, Parikh S, Denholtz M,
647 Huang Y, Yamaguchi Y, Shen H, Allayee H, Crump JG, Force TI, Lien CL, Makita T,
648 Lusis AJ, Kumar SR, Sucov HM. Frequency of mononuclear diploid cardiomyocytes
649 underlies natural variation in heart regeneration. *Nat Genet* 2017; 49: 1346-1353.
650 60. Vaughan AE, Brumwell AN, Xi Y, Gotts JE, Brownfield DG, Treutlein B, Tan K, Tan V, Liu
651 FC, Looney MR, Matthay MA, Rock JR, Chapman HA. Lineage-negative progenitors
652 mobilize to regenerate lung epithelium after major injury. *Nature* 2015; 517: 621-625.
653 61. Potapova TA, Seidel CW, Box AC, Rancati G, Li R. Transcriptome analysis of tetraploid
654 cells identifies cyclin D2 as a facilitator of adaptation to genome doubling in the presence
655 of p53. *Mol Biol Cell* 2016; 27: 3065-3084.
656 62. Neurohr GE, Terry RL, Lengefeld J, Bonney M, Brittingham GP, Moretto F, Miettinen TP,
657 Vaites LP, Soares LM, Paulo JA, Harper JW, Buratowski S, Manalis S, van Werven FJ,
658 Holt LJ, Amon A. Excessive Cell Growth Causes Cytoplasm Dilution And Contributes to
659 Senescence. *Cell* 2019; 176: 1083-1097 e1018.
660 63. Demidenko ZN, Blagosklonny MV. Growth stimulation leads to cellular senescence when
661 the cell cycle is blocked. *Cell cycle (Georgetown, Tex* 2008; 7: 3355-3361.
662 64. Lengefeld J, Cheng CW, Maretich P, Blair M, Hagen H, McReynolds MR, Sullivan E, Majors
663 K, Roberts C, Kang JH, Steiner JD, Miettinen TP, Manalis SR, Antebi A, Morrison SJ,

Lees JA, Boyer LA, Yilmaz OH, Amon A. Cell size is a determinant of stem cell potential during aging. *Sci Adv* 2021; 7: eabk0271.

65. Leach JP, Morrisey EE. Repairing the lungs one breath at a time: How dedicated or facultative are you? *Genes Dev* 2018; 32: 1461-1471.
66. Zacharias WJ, Frank DB, Zepp JA, Morley MP, Alkhaleel FA, Kong J, Zhou S, Cantu E, Morrisey EE. Regeneration of the lung alveolus by an evolutionarily conserved epithelial progenitor. *Nature* 2018; 555: 251-255.
67. Chapman HA, Li X, Alexander JP, Brumwell A, Lorizio W, Tan K, Sonnenberg A, Wei Y, Vu TH. Integrin alpha6beta4 identifies an adult distal lung epithelial population with regenerative potential in mice. *The Journal of clinical investigation* 2011; 121: 2855-2862.
68. Redente EF, Jacobsen KM, Solomon JJ, Lara AR, Faubel S, Keith RC, Henson PM, Downey GP, Riches DW. Age and sex dimorphisms contribute to the severity of bleomycin-induced lung injury and fibrosis. *American journal of physiology* 2011; 301: L510-518.
69. Chen J, Chen Z, Narasaraju T, Jin N, Liu L. Isolation of highly pure alveolar epithelial type I and type II cells from rat lungs. *Lab Invest* 2004; 84: 727-735.
70. Jansing NL, McClendon J, Kage H, Sunohara M, Alvarez JR, Borok Z, Zemans RL. Isolation of Rat and Mouse Alveolar Type II Epithelial Cells. *Methods Mol Biol* 2018; 1809: 69-82.
71. Misharin AV, Morales-Nebreda L, Mutlu GM, Budinger GR, Perlman H. Flow cytometric analysis of macrophages and dendritic cell subsets in the mouse lung. *American journal of respiratory cell and molecular biology* 2013; 49: 503-510.
72. Halliday M, Radford H, Sekine Y, Moreno J, Verity N, le Quesne J, Ortori CA, Barrett DA, Fromont C, Fischer PM, Harding HP, Ron D, Mallucci GR. Partial restoration of protein synthesis rates by the small molecule ISRIB prevents neurodegeneration without pancreatic toxicity. *Cell Death Dis* 2015; 6: e1672.
73. Flozak AS, Lam AP, Russell S, Jain M, Peled ON, Sheppard KA, Beri R, Mutlu GM, Budinger GR, Gottardi CJ. Beta-catenin/T-cell factor signaling is activated during lung injury and promotes the survival and migration of alveolar epithelial cells. *J Biol Chem* 2010; 285: 3157-3167.
74. Taghizadeh RR, Sherley JL. CFP and YFP, but not GFP, provide stable fluorescent marking of rat hepatic adult stem cells. *J Biomed Biotechnol* 2008; 2008: 453590.

Acknowledgements

This work relied on the following Northwestern University services and core facilities: Flow Cytometry (NCI CA060553, 1S10OD011996, 1S10OD026814); Center for Advanced Microscopy (NCI CCSG P30 CA060553, NCRR 1S10 RR031680, 1S10OD021704); BioCryo facility of Northwestern University's NUANCE Center (NSF ECCS-2025633, DMR-1720139).

Funding: MH is supported by AR073270, AM is supported by HL135124, HL153312, AG049665 and AI135964; GRSB is supported by ES13995, HL071643, AG049665; CJG is supported by HL134800, AR073270 and GM129312. All authors declare no competing financial interests.

Author contributions: AW, MMH, SW, ASF, LW and RPA designed and conducted experiments; AW, MMH, ASF, AM and CJG analyzed results; RG wrote a macro for image analysis; AM advised and analyzed flow cytometry, SH, LD, MH, AM, GRSB advised and discussed results; CJG designed and supervised study, performed analysis and wrote manuscript. MH, AM, GRSB and CJG provided funding for project.

715 **Figures**

716

717 **Figure 1**: **Lung injury induces AT2 cell hypertrophy.** (**A**) Schematic of experimental design.
718 Young adult *Sftpc*^{CreER}; Lox-Stop-Lox^{ZsGreen} mice (3-5 months) received 10mg of tamoxifen via
719 oral gavage 22 days prior to administration of bleomycin (0.025 units, i.t.). Lungs from saline
720 (control) and bleomycin-treated mice were harvested on Day 10, fixed and processed for frozen
721 sectioning and immunofluorescence analysis. (**B**) Representative lung sections showing native
722 GFP fluorescence from AT2-lineage label and immunofluorescence staining of AT1 cells by
723 podoplanin (Pdpn, magenta). Scale bar = 50μm. Note lineage-labeled AT2 cells appear larger
724 after bleomycin injury. (**C**) Graph shows quantification of AT2 cell area and perimeter using
725 image analysis in FIJI (workflow in Fig. S1A). Data points are from two mice, 5 fields of view per
726 condition. Mean +/- SD. $p < 0.0001$ by t-test. (**D**) Quantification of lineage-labeled AT2 cell
727 volumes using cleared, 200μm thick-section optical z-stack imaging (Imaris). Data points are
728 from three saline and two bleomycin-injured mice. Mean +/- SD; $p = 0.0072$ by t-test.
729 Representative fields of view in Supplemental Video 1. To ensure robustness and increase N's,
730 injury-induced cell size increase also validated by flow cytometry in Fig. S2.

731

732

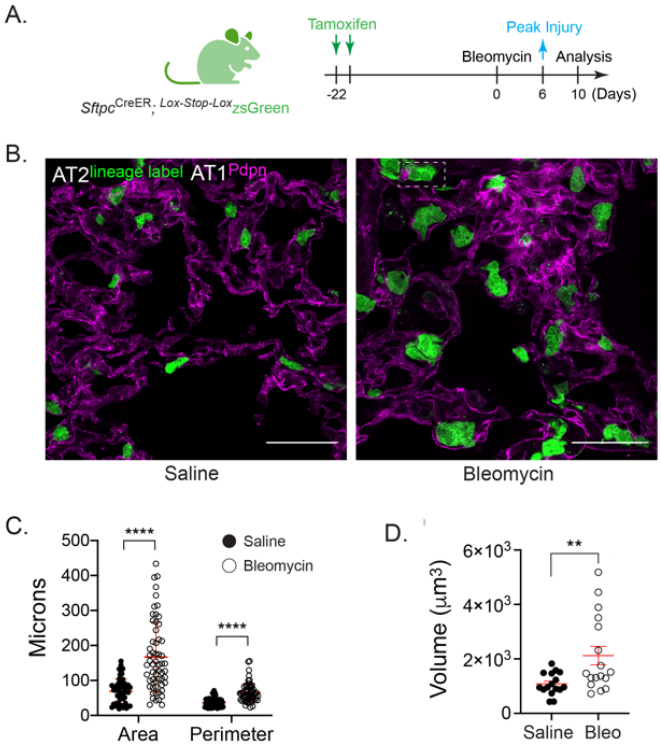

733

734 **Figure S1**: **AT2 cell hypertrophy by frozen- and thick-section image analysis**. (**A**) Black
735 and white mask of images in Figure 1 for quantification of lineage-labelled AT2 cell area and
736 perimeter (black objects, green arrow). (**B**) Injury-induced AT2 hypertrophy readily observed by
737 frozen sections, which are ~4-fold thicker than typical paraffin sections. (**C**) Hypertrophic AT2
738 phenotype is not an artefact of lineage-labeling AT2 cells. Confocal image of Vibratome-cut
739 200μm thick lung section from a C57BL/6 mouse with clearing (SHIELD method)
740 immunofluorescence detection of SpC (red) and nuclei (Draq5; cyan). Note bleomycin-treated
741 AT2 cells are clearly larger, even 21 days post-bleomycin instillation.
742
743
744

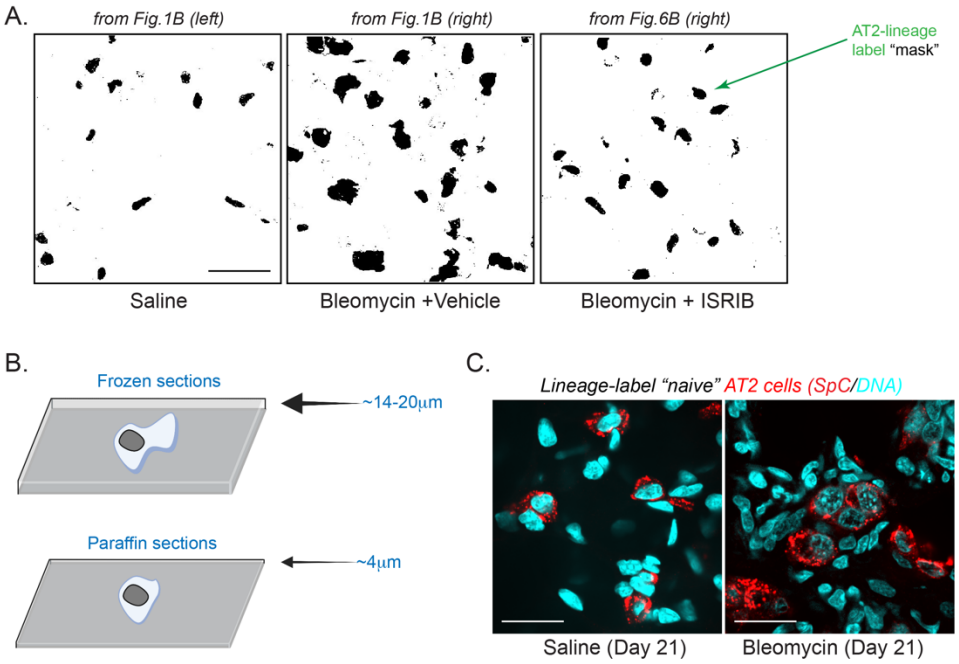

745

Figure 2: **Lung injury induces polyploidization of lineage-labeled and SpC+ AT2 cells**. (**A**) Schematic of experimental design as in Fig.1. Representative confocal images of lung sections from bleomycin-treated mice; two independent fields of view from low and high-magnification insets (boxed region) are shown (a' and a"). Native GFP fluorescence from AT2-lineage label and immunofluorescence staining of AT1 cells by podoplanin (Pdpn, magenta). DNA labeling by Hoechst (gray). Scale bar = 50μm and 10 μm for inset. Asterisks show suspected binucleated AT2 cells. Arrows show plan of optical z-section, revealing that nuclei appear to touch in these cells. Magenta arrow in a' indicates podoplanin signal. It is not possible in this image to know if podoplanin labels the binucleated AT2 or an adjacent AT1 cell (see Fig. 6D for evidence of binucleated/podoplanin positive cell). SpC+ binucleated AT2 cells are shown in Fig. S2F. (**B**) Graph shows quantification of AT2 cell binucleation. Data points are from three mice (different symbol colors/mouse), 5-8 fields of view per condition. Note the binucleation rate for one mouse (gray circles) was quantified 21 days post-bleomycin, showing persistence of binucleation through this time point. Mean +/- SD in red. $p < 0.0001$ by t-test. Injury-induced binucleation was also interrogated by flow cytometry in Fig. S2A-E.

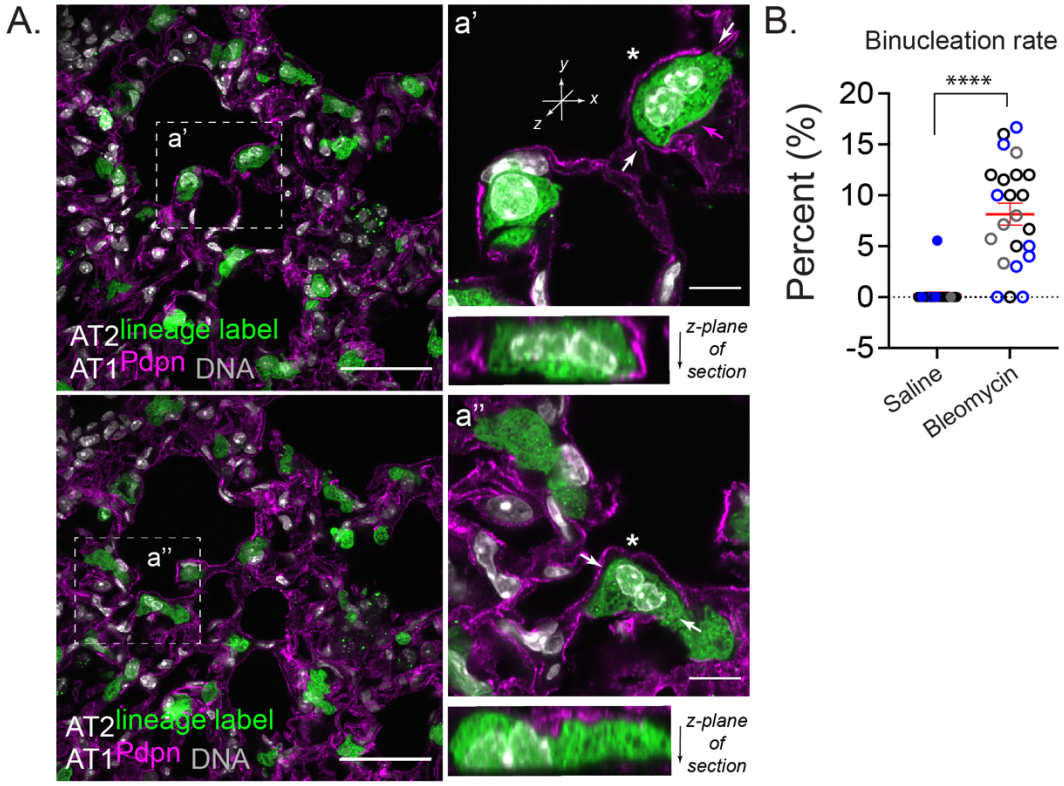

765 **Figure S2**: **Quantification of injury-induced AT2 hypertrophy and binucleation by flow**
766 **cytometry**. (**A**) Schematic of experimental design. (**B**) Young adult mice (3-5 months) were
767 administered saline alone or 0.025 units of bleomycin and lungs were harvested and digested
768 for flow cytometry on Day 12 with representative flow plots gated on CD45-/EpCAM+ AT2 cells
769 with 2N (diploid, red) or 4N DNA content (cyan) (Methods). (**C**) Quantification of AT2 cell size
770 (median Forward Scatter Area). (**D**) Percent 2N versus 4N AT2 cells. N = 3 mice. p = 0.0008
771 and 0.0039 by ANOVA with Tukey's. (**E**) Validation of bleomycin-induced AT2 cell size increase
772 and binucleation by cytospin analysis. Cellular F-actin stained with phalloidin (green) to
773 distinguish *bona fide* binucleation, with absence of F-actin-rich cell-cell junction between nuclei.
774 (**F**) Binucleated AT2 cells can be SpC+. Confocal z-stack image of Vibratome-cut 200μm thick
775 lung section from a C57BL/6 mouse with clearing (SHIELD method) immunofluorescence
776 detection of SpC (red) and nuclei (Draq5; cyan). Double arrowhead implicates two binucleated
777 AT2 cells in the same field of view.
778
779

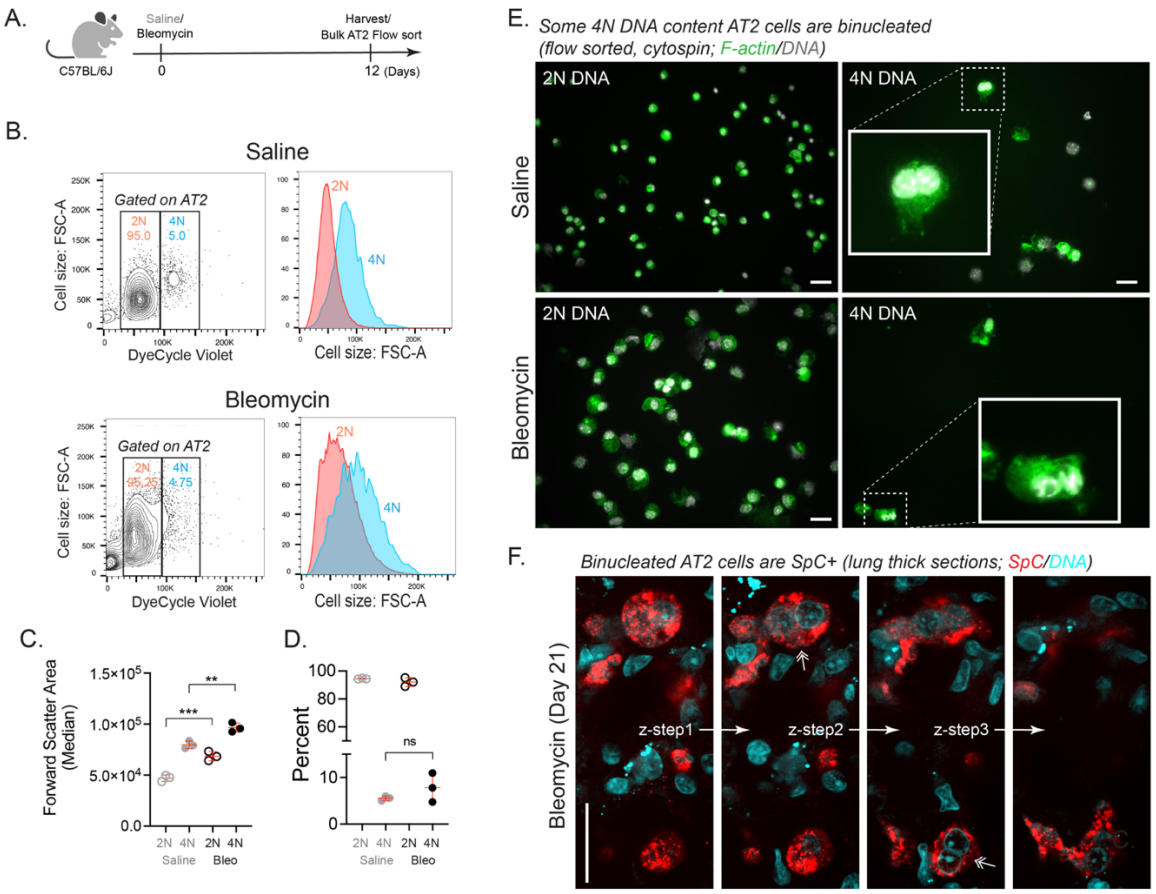

780

Figure 3: **AT2 cell binucleation is not universally associated with Krt8-high expression phenotype.** (**A**) Schematic of experimental design as in Fig.1. Confocal image of lung section from bleomycin-treated mice; same image as Figure 2A, now including Krt8 immunofluorescence channel (cyan). Asterisk denotes binucleated AT2 cell with normal levels of Krt8 protein. Native GFP fluorescence from AT2-lineage label and immunofluorescence staining of AT1 cells by podoplanin (Pdpn, magenta). DNA labeling by Hoechst (gray). (**B**) Confocal image of binucleated Krt8-high cell (asterisk) lacking AT2 lineage-label. Scale bar = 50μm and 25 μm for inset. (**C**) Confocal image of lineage-labeled binucleated AT2 cell adjacent to lineage negative mononuclear Krt8-high cell (z-stack not shown). Scale bar = 25μm.

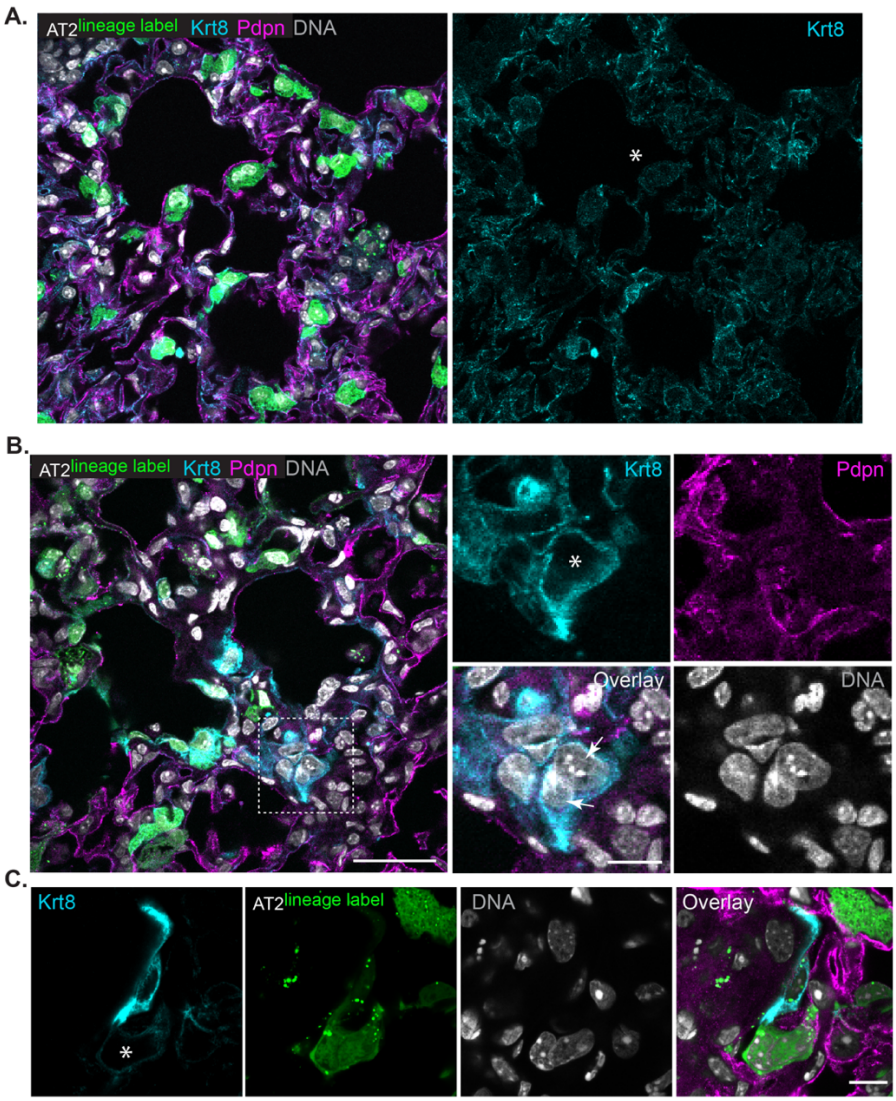

794 **Figure S3: Identification of rare ≥4N AT2 cells via stochastic multi-color Confetti-labeling**
795 **system.** (**A**) Schematic adapted from (39) using *Sftpc*$^{\text{Cre-ER; R26R-Confetti}}$ strain (14). (**B**) Tamoxifen
796 activation of *Sftpc*-targeted lineage-label at days 6-7 post-bleomycin injury and harvested Day
797 21. (**C**) Confocal image of thick-section cleared (SHIELD) lung, maximum z-projection of 3
798 slices showing rare YFP (green)/RFP (magenta) dual-positive cells, suggesting mononuclear
799 polyploidy from partial nuclear exclusion of signal. The enlarged/flattened size of this cell
800 (>25μm) is also compatible with 4N polyploidy. (**D**) Lower magnification view maximum z-
801 projection (40 planes) shows that most lineage labeled cells are either nuclear GFP (nGFP),
802 YFP (cytoplasmic) or RFP positive, with very few nGFP or YFP and RFP-dual-positive cells (see
803 inset showing gray cell, which reflects overlay of YFP (green) and RFP (magenta) signals). As
804 this cell is ~10μm, it likely reflects a G2-phase AT2 cell with 4N DNA content. Asterisk validates
805 bleomycin injury showing RFP lineage label along flattening AT1 cells. (**E**) Quantification of C-
806 D from n = 2 mice/condition. Note our microscopes do not discriminate between nGFP/YFP
807 signals, due to spectral overlap of these fluorescent proteins. Fortunately, distinguishing
808 between nGFP/YFP is not critical to answer the polyploidy question—as nGFP or YFP *and* RFP
809 is sufficient evidence of >2N DNA content, where we see this combination only rarely (~1-2%).
810 Few nGFP cells are detected when we activate the lineage label shortly after peak injury (Days
811 6, 7 versus 14, 15), possibly due to nuclear nGFP toxicity (74). Lastly, CFP cells are typically
812 detected less frequently with this reporter, possibly due to its placement in the cassette (39).

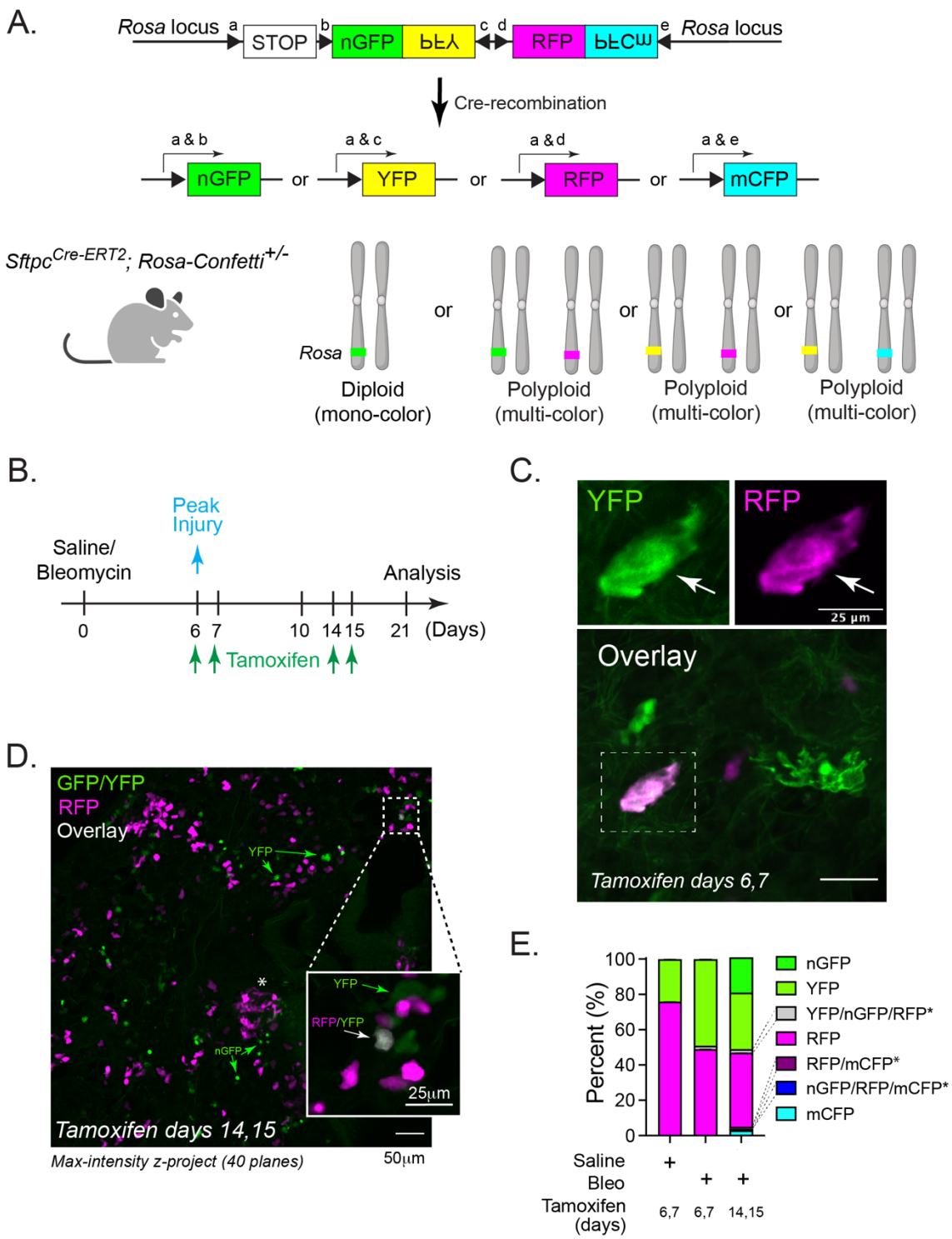
A.
Rosa locus
STOP
nGFP
RFP
Rosa locus
Cre-recombination
a & b
a & c
a & d
a & e
nGFP
YFP
RFP
mCFP
or
Sftpc Cre-ERT2; Rosa-Confetti +/-
Rosa
Diploid (mono-color)
Polyploid (multi-color)
Polyploid (multi-color)
Polyploid (multi-color)
B.
Peak Injury
Saline/ Bleomycin
Analysis
0
6 7
10 14 15
21 (Days)
Tamoxifen
C.
YFP
RFP
25 µm
Overlay
Tamoxifen days 6,7
D.
GFP/YFP
RFP
Overlay
YFP
nGFP
RFP/YFP
25µm
Tamoxifen days 14,15
Max-intensity z-project (40 planes)
50µm
E.
Percent (%)
100
80
60
40
20
0
nGFP
YFP
YFP/nGFP/RFP*
RFP
RFP/mCFP*
nGFP/RFP/mCFP*
mCFP
Saline
Bleo
Tamoxifen (days)
6,7
6,7
14,15

813

814 **Figure 4**: **Binucleation is a feature of murine AT2 cell cultures and organoids.** (**A**) Top:
815 Confocal images of mouse AT2 cells grown 4 days on glass and rat AT2 cells grown 10 days on
816 filters. Cells were fixed and stained with Hoechst (DNA in cyan or gray), phalloidin (F-actin,
817 green), Krt8 (green) or β-catenin (red) as indicated. Top: Arrows (white) indicate two nuclei
818 "kissing" without an intervening junction (by F-actin or β-catenin staining). Bottom: Dotted lines
819 (white) outline binucleated cells. (**B**) Schematic for activation of AT2-lineage label before AT2
820 isolation for organoid growth. (**C**) AT2 cell (green), F-actin (magenta) and DNA (gray) with
821 lineage-labeled binucleated cell (arrow). (**D**) Rate of AT2 binucleation in organoids. Scale bars =
822 50μm.
823

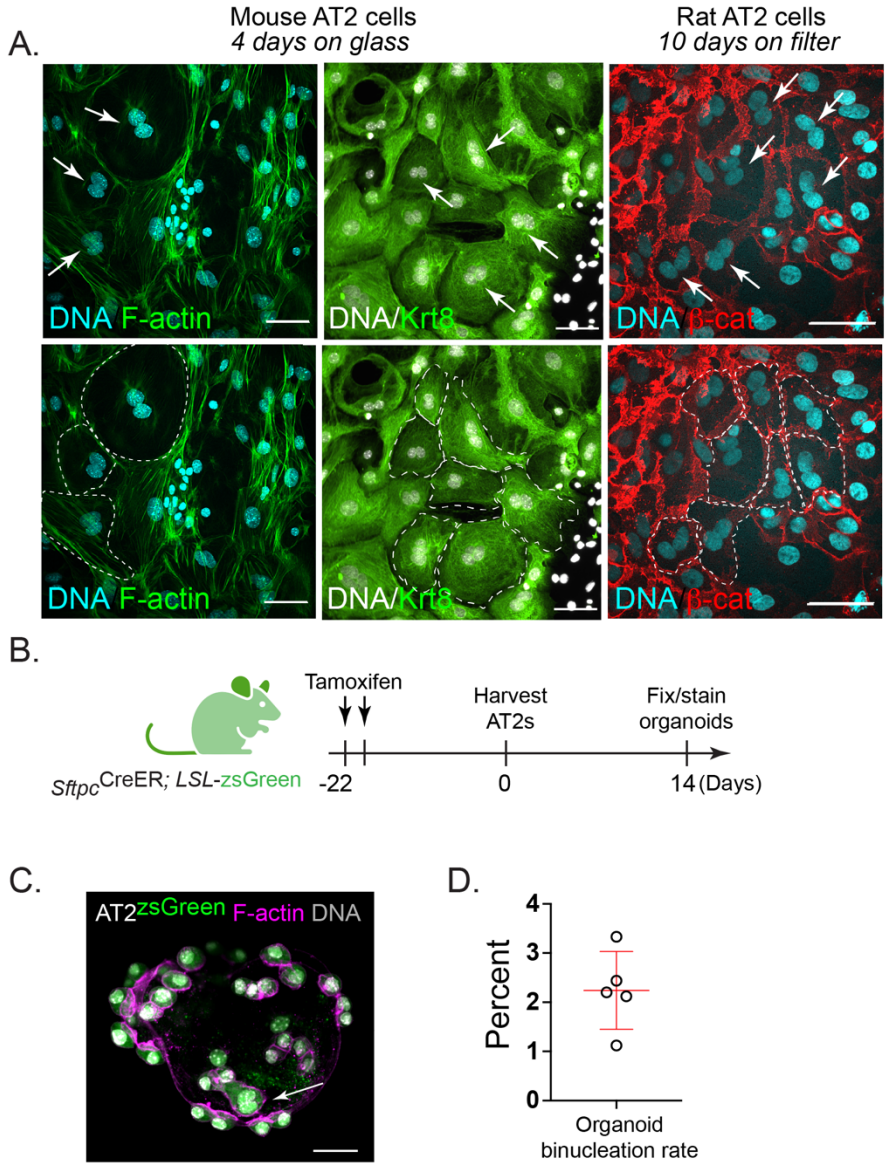

824

825 **Figure S4: Detection of binucleated, lineage-labeled mouse AT2 cells in cell culture**
826 (**A**) Schematic for activation of AT2-lineage label before AT2 isolation. (**B**) Confocal image of
827 lineage-labeled AT2 cell (yellow) grown 3 days on glass. Arrow indicates binucleated, AT2-
828 derived cell. F-actin in cyan.
829
830

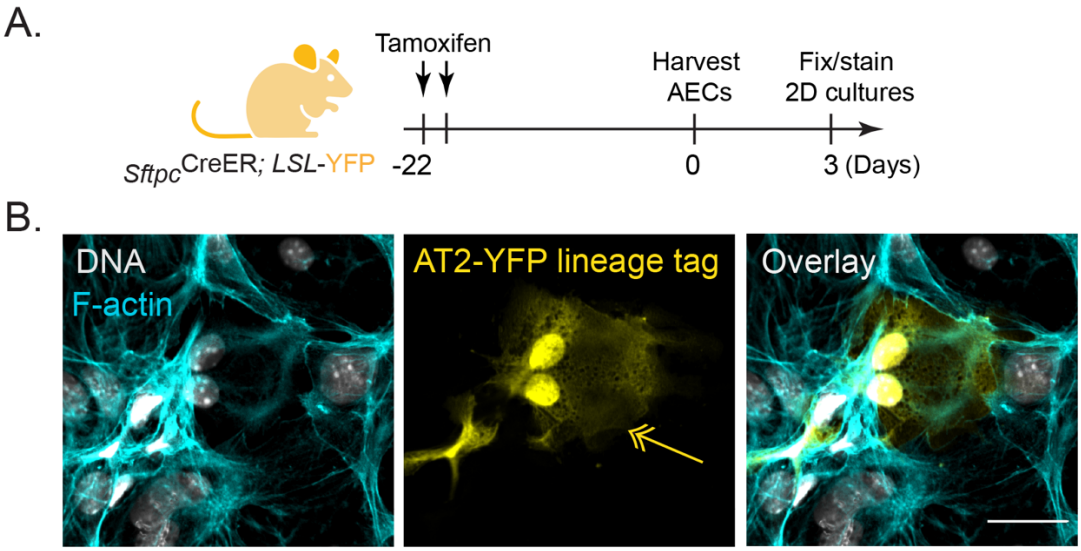

831
832
833
834
835
836

837 **Figure 5**: **AT2 cell binucleate via failed cytokinesis.** Mouse AT2 cells were isolated and
838 phase-contrast live-imaged every 15-minutes (Methods). Time stamp and evident cell-cycle
839 phases are shown in cyan. Arrow indicated dividing cell.

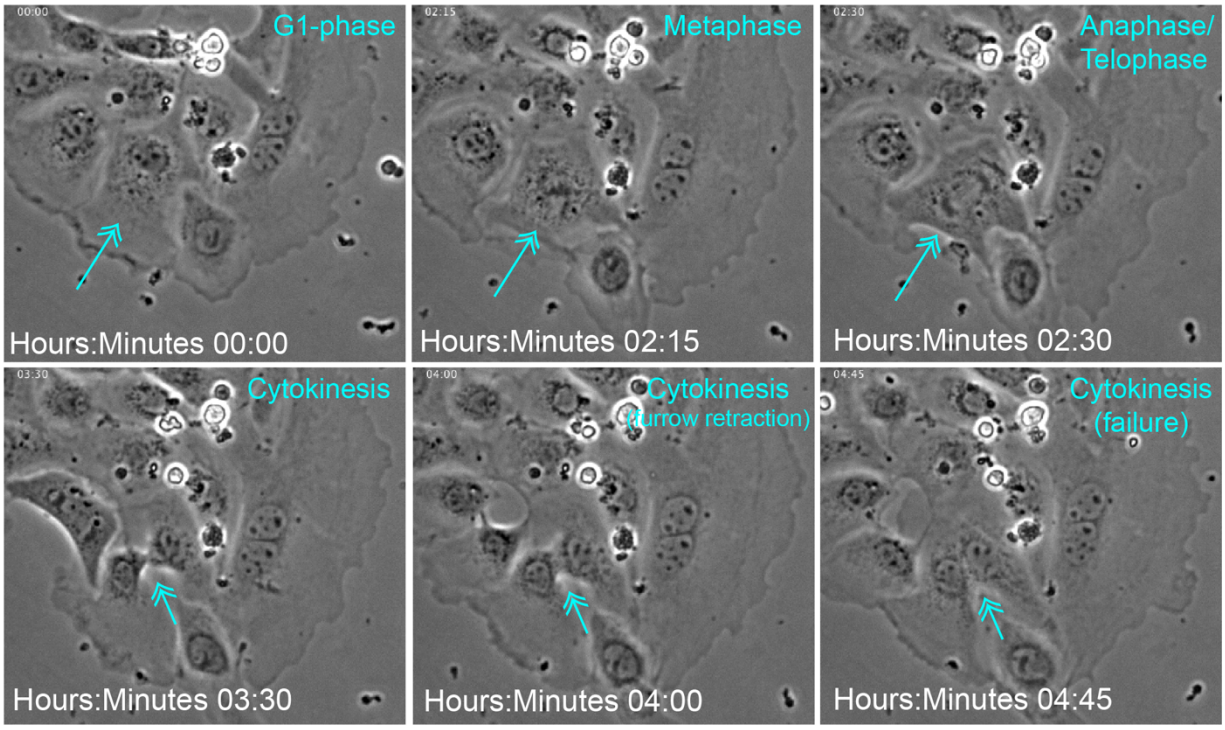

840

841 **Figure 6**: **ISRIB limits AT2 hypertrophy and polyploidy cell-autonomously**. (**A**) Schematic
842 for AT2 lineage-trace before bleomycin-injury with and without ISRIB therapy. (**B**) Confocal
843 images of fixed frozen lung sections with native zsGreen and immunofluorescence of AT1
844 marker, podoplanin. Scale 50μm. (**C**) Scatter plot of zsGreen object sizes by FIJI as described
845 in Figure S1. Graph identical to Fig.1C with ISRIB data added. Significance by ANOVA. (**D**)
846 Epifluorescence overlay images of mouse AT2 cell Day2-cultures incubated with Vehicle/ISRIB
847 (0.025μm) through Days 4-5. Arrows (magenta) show podoplanin+ binucleated cells that are
848 peripheral to large flat bi-/tri-nucleated cells with diminishing podoplanin and high levels of β-
849 catenin (white arrow). Scale 50μm. (**E**) Nuclear area (DNA) measurements by ImageJ as proxy
850 for cell size allowed for unbiased analysis. N = 6829 (Vehicle) and 7387 (ISRIB) nuclei
851 measured. Data averaged from 3 independent AT2 isolations for cells quantified at 48 and 72-
852 hours +/- ISRIB. p < 0.0001**** by Mann-Whitney test. (**F**) Histogram of data in **E**. (**G**)
853 Binucleation events quantified as from 44 (Vehicle) and 43 (ISRIB) fields of view. p = 0.035* by
854 Mann-Whitney test. Dotted red lines reflect median, first and third quartiles.

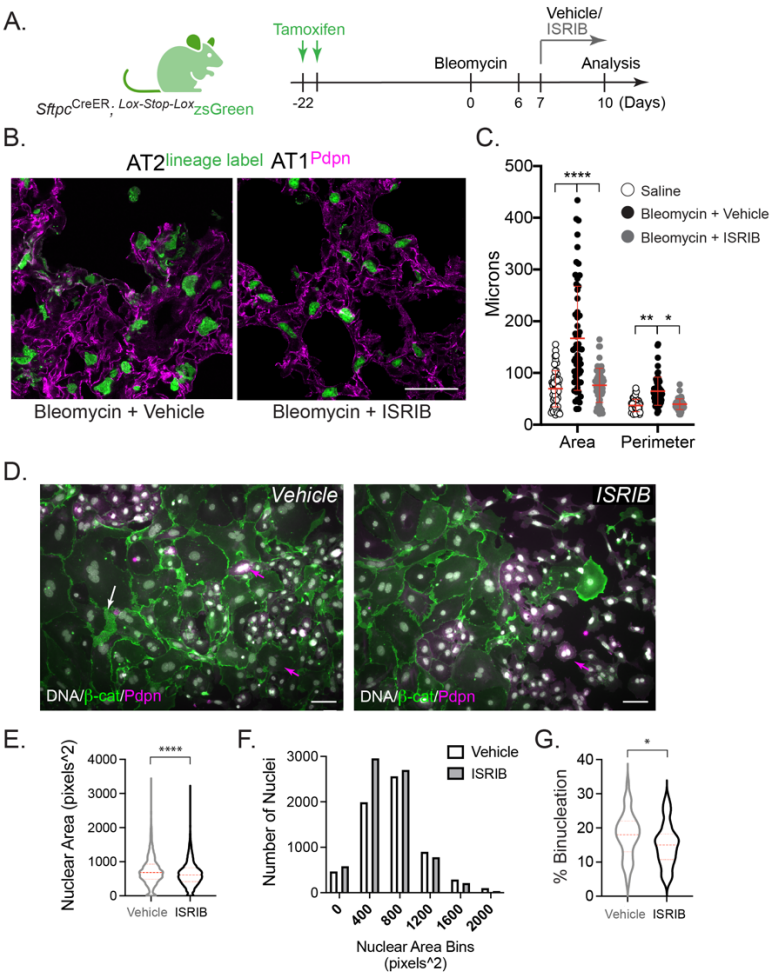

855

856 **Figure S5: Antibody-isotype control to validate podoplanin staining in ex vivo mouse AT2**
857 **cell cultures.** Individual fluorescence panels from overlay images in Figure 6D.
858

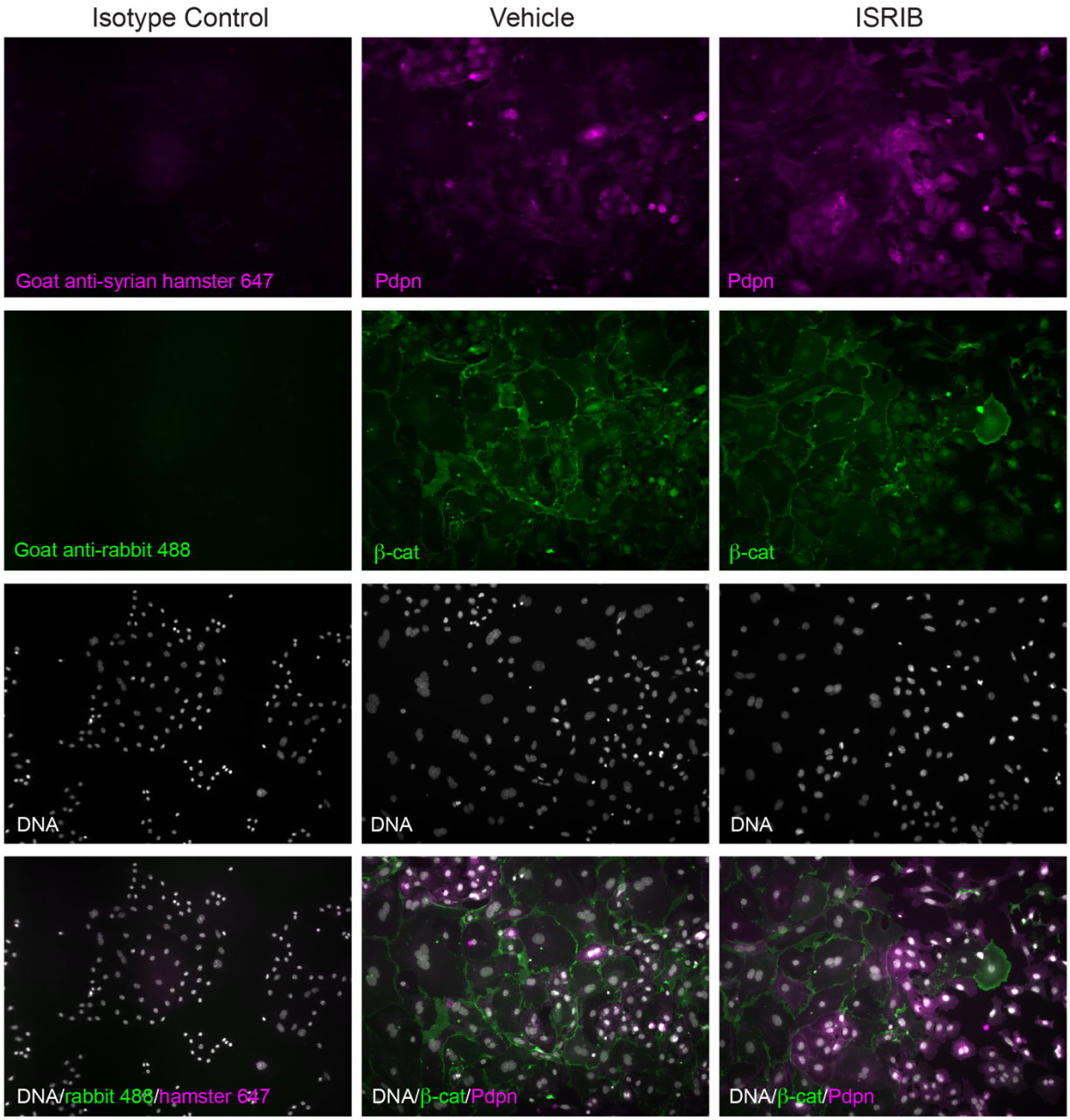

859

860 **Figure 7**: **Model for alveolar epithelial stress-induced hypertrophy and polyploidization in**
861 **lung injury and repair.** (**A**) AT2 "aberrant" repair (dotted blue line) due to persistent ISR, AT2
862 hypertrophic growth, cytokinesis failure and stalled AT2-to-AT1 cells (right). (**B**) ISRIB therapy
863 (dotted pink line) restores ISR to levels for normal AT2-to-AT1 growth, division and
864 differentiation (dotted gray line). Schematic with BioRender software.
865
866

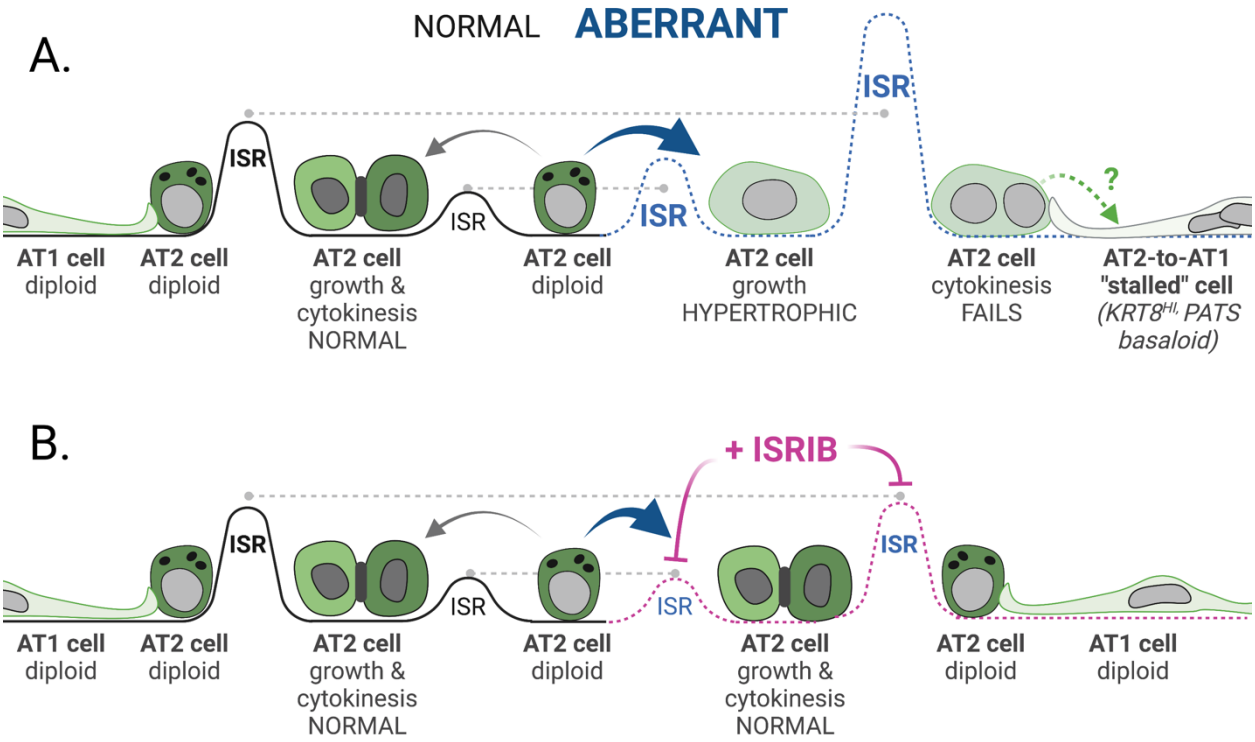

867
868
869